

1 **Multi-spectral and multi-instrument observation of TIDs**
2 **following the Total Solar Eclipse of August 21, 2017**

3 **Saurav Aryal¹, George Geddes¹, Susanna C. Finn¹, Sebastijan Mrak², Ivan Galkin¹, Ingrid**
4 **Cnossen^{3,4}, Timothy Cook¹, and Supriya Chakrabarti¹**

5 ¹Lowell Center for Space Science and Technology (LoCSST), Department of Physics and Applied Physics, University of
6 Massachusetts Lowell, Lowell, MA

7 ²Department of Electrical and Computer Engineering and Center for Space Physics, Boston University, Boston, MA, USA

8 ³Department of Climate and Space Sciences and Engineering, University of Michigan, Ann Arbor, MI, USA

9 ⁴British Antarctic Survey, Cambridge, UK

10 **Key Points:**

- 11 • Meridional and vertical wave properties of Large Scale Travelling Ionospheric Distur-
- 12 bances (LSTIDs) are characterized based on multi-instrument observations
- 13 • While the observed LSTIDs are generated by geomagnetic effects, effects of the solar
- 14 eclipse that preceded the LSTID are also studied based on modeling
- 15 • Model estimates suggest that the Ionosphere-Thermosphere system was precondi-
- 16 tioned due to the eclipse but there is no evidence of this preconditioning affecting the
- 17 LSTIDs

This is the author manuscript accepted for publication and has undergone full peer review but has not been through the copyediting, typesetting, pagination and proofreading process, which

may lead to differences between this version and the Version of Record. Please cite this article as doi: [10.1029/2018JA026333](https://doi.org/10.1029/2018JA026333)

Abstract

Wave-like structures in the upper atmospheric nightglow brightness were observed on the night of August 22, 2017, approximately 8 hours following a total solar eclipse. These wave-like perturbations are signatures of Atmospheric Gravity Waves (AGWs) and associated Traveling Ionospheric Disturbances (TIDs). Observations were made in the red line (OI 630.0 nm) and the green line (OI 557.7 nm) from Carbondale, IL, at 2–10 UTC on August 22, 2017. Based on wavelet analyses, the dominant time period in both the red and green line was around 1.5 hours. Differential Total Electron Content (DTEC) data obtained from GPS TEC measurements at Carbondale, IL, and ionospheric parameters from digisonde measurements at Idaho National Laboratory and Millstone Hill showed a similar dominant time period. Based on these observations and their correlation with geomagnetic indices, the TIDs appear to be associated with geomagnetic disturbances. In addition, by modeling the Ionosphere-Thermosphere (IT) system's response to the eclipse, it was seen that while the eclipse enhanced the O/N_2 ratio and electron density (N_e) at 250 km, it did not affect the TIDs. Vertical (7 m/s) and meridional (616 m/s) phase velocities of the TIDs were estimated using cross-correlation analysis between red and green line brightness profiles and spectral analysis of the DTEC keogram, respectively. This provides a method to characterize the three dimensional wave properties of TIDs.

1 Introduction

Atmospheric Gravity Waves (AGWs) manifest as Traveling Ionospheric Disturbances (TIDs) via ion-neutral coupling in the Ionosphere-Thermosphere (IT) system [Hines, 1960]. TIDs are wave-like plasma oscillations in the ionosphere that can be triggered by various processes (including AGWs) and occur at different temporal and spatial scales. TIDs with wavelengths of 100–300 km are classified as Medium Scale TIDs (MSTIDs) and can be caused by various processes, but in general are associated with tropospheric forcing [Kelley, 2011]. TIDs with wavelengths larger than 1000 km and with time periods greater than one hour are classified as Large Scale TIDs (LSTIDs) [Hocke *et al.*, 1996].

Most LSTIDs propagate from either pole and are associated with magnetic disturbances. Geomagnetic storms cause rapid enhancement of the auroral electrojet that leads to thermospheric heating and expansion [Davis, 1971; Chimonas and Hines, 1970b]. This generates AGWs that propagate toward the equator. The divergence of AGWs in turn generates LSTIDs [Prölss and Očko, 2000]. LSTIDs that have propagated equatorward and are

50 associated with geomagnetic storms have been observed by previous studies [*Habarulema*
51 *et al.*, 2018, and references therein]. For example, based on magnetometer measurements,
52 *Habarulema et al.* [2018] showed that equatorward TIDs were launched following a south-
53 ward turning of the Interplanetary Magnetic Field (IMF).

54 Besides geomagnetic storms, solar eclipses are also known to excite AGWs [e.g., *Liu*
55 *et al.*, 1998; *Chimonas and Hines*, 1970a], that alter the IT system [*Lin et al.*, 2018; *Harding*
56 *et al.*, 2018]. *Liu et al.* [1998] conclude that the ionospheric perturbations that they observed
57 using ionosondes during the total solar eclipse of October 24, 1995 were most likely due to
58 plasma up-flow and down-flow induced by rapid temperature increase immediately following
59 the eclipse.

60 The August 21, 2017 solar eclipse occurred over the continental USA (from the west
61 to the east coast) where numerous satellite receivers and ground based instruments were
62 present, leading to an abundance of data for studying the effects on the upper atmosphere.
63 *Coster et al.* [2017] found signatures of possible mountain waves, using Total Electron Con-
64 tent (TEC) maps, during the August 21, 2017 eclipse. Furthermore, for the same eclipse
65 event, *Goncharenko et al.* [2018] used co-located measurements of digisonde and the Mill-
66 stone Hill ISR (Westford, MA, ~ 60% peak obscuration), and observed a fast (20-40 m/s)
67 upward plasma drift above the peak height of the F2 layer, hmF2, immediately following the
68 maximum obscuration which they attributed to rapid temperature increase. Neutral wind
69 velocity derived from night-time OI 630.0 nm (red line) emission measurements by a Fabry-
70 Perot Interferometer (FPI) in Brazil showed perturbations in neutral winds far from the path
71 of the August 21, 2017 eclipse. Global-scale simulations using a UV obscuration mask that
72 mimicked the August 21, 2017 eclipse's effect on the upper atmosphere successfully pre-
73 dicted the measured changes (using the red line) in neutral wind qualitatively [*Harding et al.*,
74 2018].

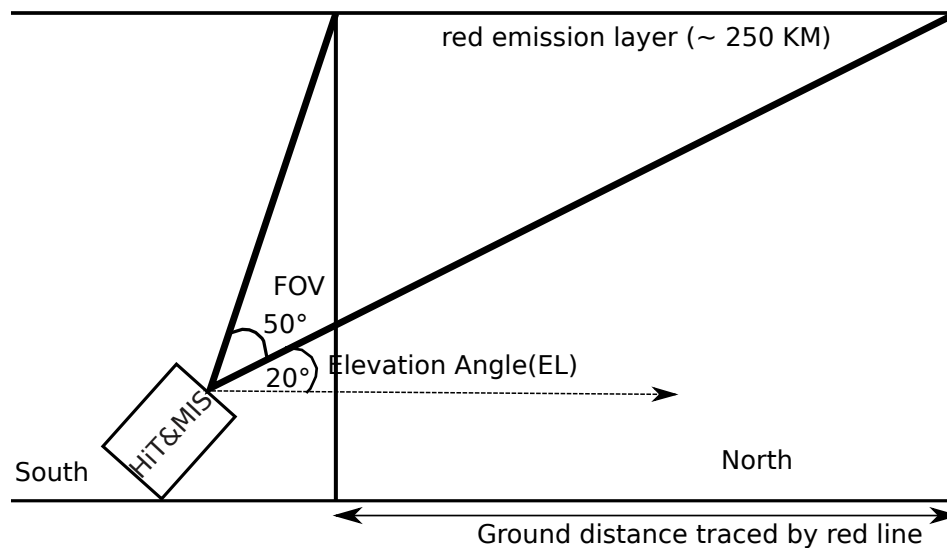
75 On August 22, 2017 a sequence of LSTIDs was observed in the northern hemisphere,
76 following a minor geomagnetic storm (minimum Dst index ~-30 nT, peak Auroral Electrojet
77 index ~1000 nT) over North America. The geomagnetic storm followed the eclipse of Au-
78 gust 21, 2017 that occurred hours earlier. In this paper, we present a comprehensive LSTID
79 analysis, by virtue of simultaneous measurements by: ground-based spectral imager (at Car-
80 bondale, IL which was in the path of totality), Global Positioning System (GPS) differential
81 TEC maps, and ionospheric parameters derived from digisonde. We describe the TID event

82 analysis in detail and characterize the TID wave parameters. In addition, we compare our ob-
 83 servations to simulations with the Global Ionosphere-Thermosphere Model (GITM) [Ridley
 84 *et al.*, 2006] to examine if the solar eclipse may have affected the observed TIDs.

85 2 Measurements

86 2.1 Spectral measurements

87 Our observations of the TIDs from Carbondale, IL (Geographic location: 37.7°N,
 88 89.2°W) were made using the High Throughput and Multi-slit Imaging Spectrograph (HiT&MIS)
 89 [Chakrabarti *et al.*, 2012]. HiT&MIS can simultaneously measure six upper atmospheric
 90 emission features at high resolution (dispersion of ~ 0.02 nm/px in red line, for example).
 91 The field-of-view (FOV) of HiT&MIS is approximately 0.1° by 50° and was centered at an
 92 elevation angle of 45° looking towards the northwest (Figure 1). The spectral images were
 93 recorded at a cadence of 4 minutes using a Charged Coupled Device (CCD) camera during
 94 2–10 UTC on August 22, 2017. Simultaneous measurements in the red line and OI 557.7 nm
 95 (green line) are used for this particular study.

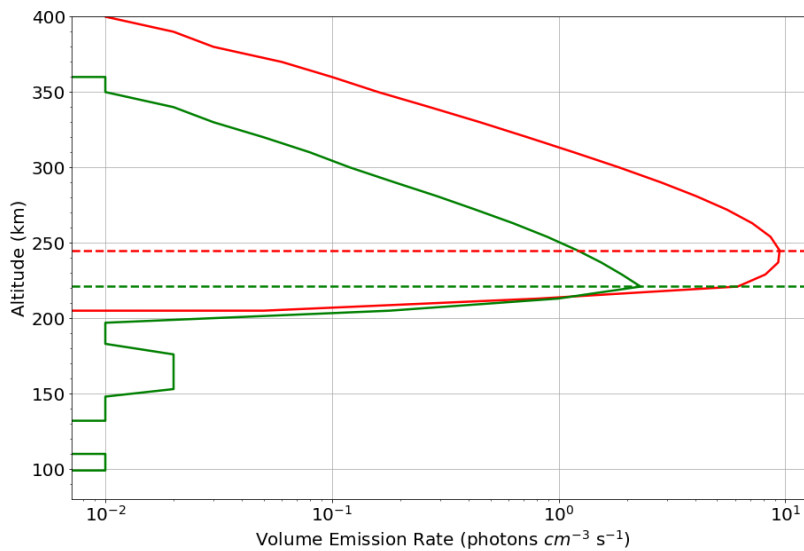


96 **Figure 1.** Viewing geometry of the HiT&MIS instrument on August 21-22, 2017 at Carbondale, IL. The
 97 latitudes (and ground distance) traced by the red line are shown assuming the peak emission height of 250 km.

98 From the raw CCD images, wavelength regions around the red and green lines, plus
 99 a diagnostic cloud indicator also observed by HiT&MIS, were extracted as a function of
 100 HiT&MIS elevation angle and wavelength. The NeI 630.5 nm line (present in street lights)

101 was used as an indicator of cloud activity as reflection of street lights from clouds acts as a
 102 proxy for sky conditions. See *Aryal et al.* [2018] for a more detailed description of the spec-
 103 tra extraction procedure for HiT&MIS.

107 For each feature at each time-stamp, we obtained the brightness by co-adding signals
 108 from all wavelength bins around ± 0.3 nm from the line center. We then plotted the bright-
 109 ness as a function of elevation angle and time. GLObal airglOW (GLOW) [*Solomon et al.*,
 110 1988; *Solomon and Abreu*, 1989; *Bailey et al.*, 2002] model estimates of the Volume Emis-
 111 sion Rate (VER, Figure 2) provided the peak heights of the red (250 km) and green (220 km)
 112 lines in the nighttime thermosphere (Figure 2). Using these emission heights and the view-
 113 ing geometry of HiT&MIS, the elevation angles were then converted to the latitude of the
 emission height projected on the ground.



104 **Figure 2.** The Volume Emission Rate (VER) for the red and the green lines as modeled by GLOW at
 105 4 UTC on August 22, 2017. MSIS00 and IRI-90 empirical parameters were used for neutral and plasma
 106 profiles, respectively.

114

115 2.2 GPS Differential TEC measurements

116 In order to compare the airglow brightness morphologies in the spectral data, we used
 117 the differential Total Electron Content (DTEC) maps. We used Continuously Operating Ref-

118 erence Stations (CORS, www.ngs.noaa.gov/CORS) and Crustal Dynamics Data Information
119 System (CDDIS, cddis.nasa.gov) publicly available databases with Global Navigation Satel-
120 lite Systems (GNSS) observation data. This accounted for a total of ~ 1800 receivers in the
121 continental US.

122 To compute the phase-corrected slant TEC estimates, we used the approach of *Coster*
123 *et al.* [1992]. The slant TEC was converted to the vertical TEC (vTEC) via a mapping func-
124 tion applied at 300 km altitude [*Klobuchar*, 1987]. We then subtracted the background vTEC
125 to obtain DTEC residuals, using variable orders of polynomials [cf. *Mrak et al.*, 2018a]. The
126 carrier phase based differential approach provides an accuracy better than 0.03 TECu [*Coster*
127 *et al.*, 2012] ($1 \text{ TECu} = 10^{16} \text{e}^-/\text{m}^2$), which enables one to resolve tiny but spatially coherent
128 perturbations in TEC. The DTEC residuals were mapped to a geographical map at an alti-
129 tude of 300 km and transformed from the naturally irregular spatial grid into a regular grid
130 [e.g., *Azeem et al.*, 2015; *Mrak et al.*, 2018a] with a resolution of $0.2^\circ \times 0.2^\circ$ (geographical
131 coordinates). Due to the size of the grid (spatial sampling) and slant-to-vertical mapping un-
132 certainty, the minimum scale sizes that can be inferred from these maps are on the order of
133 100 km. For example, *Mrak et al.* [2018b] demonstrated detection of TIDs at wavelengths of
134 200-300 km. We extracted the DTEC time series observations for locations aligned with the
135 HiT&MIS FOV at the assumed altitude.

136 2.3 Digisonde measurements

137 An additional insight into the nature of observed TIDs is provided by the Global Iono-
138 sphere Radio Observatory (GIRO) [*Reinisch and Galkin*, 2011], a network of *ionosondes*,
139 high-frequency (HF) bottomside ionosphere sounders. We selected two GIRO locations op-
140 erated by Idaho National Laboratory at Idaho Falls, ID (INL, 43.5°N , 112°W) and by Uni-
141 versity of Massachusetts Lowell at MIT Haystack Observatory, Millstone Hill (MH, 42.5°N ,
142 71.4°W). Both observatories employed the latest Digisonde model DPS4D [*Reinisch et al.*,
143 2009; *Lowell Digisonde International*, 2018] in its high-cadence campaign mode, recording
144 the vertical sounding ionograms once a minute.

145 Since the first report of the TID phenomenon detected by means of HF radio inter-
146 ferometry [*Munro*, 1950], ionosondes have been used as reliable TID detectors with well-
147 established sensitivity to plasma perturbations, as even minute changes of the electron den-
148 sity cause easily detectable variability of the signal propagation path in the ionosphere. For

our investigation, we used time series of the Maximum Usable Frequency (MUF) at a distance of 3000 km (D), MUF(D)F₂, an URSI-standard ionogram-derived characteristic. MUF(D)F₂ (referred to as MUF hereafter) is obtained numerically using the shape of the O-wave signal trace extracted from the vertical ionogram [see *Davies, 1989*, for details] and its change reflects variability in both peak density and height of the F₂ layer (see Supplementary Figure 1). This thus enhances the overall sensitivity to plasma perturbations in comparison to individual analysis of the ionospheric characteristics describing density, reflection height, or columnar content of the ionosphere. The efficiency of the ionogram-derived MUF variation analysis for TID diagnostics was recently the subject of a multi-instrument cross-validation study as a part of the TID warning and mitigation project TechTIDE [*Altadill et al., 2018*].

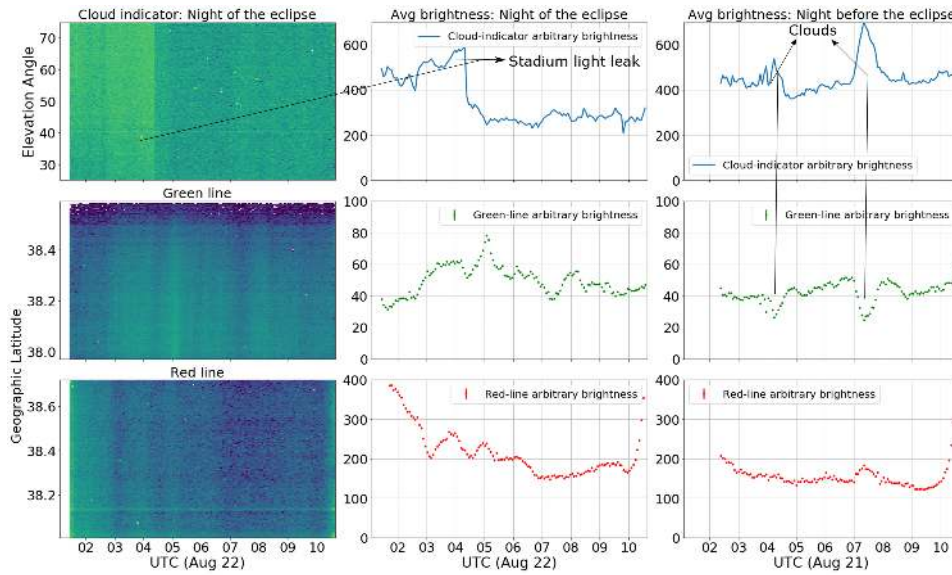
3 Results

3.1 Spectral Data

The red and green line brightnesses for the night of the eclipse and TID event (August 22, 2017) are presented in Figure 3. The brightness data for the night before the eclipse (August 21, 2017) are also shown for comparison. The red and green line brightnesses on the night with the TID event (August 22) show wave-like brightness perturbations, while the perturbations on the night before (August 21) only coincide with the cloud-indicator, especially in the green line. A slightly positive coincidence is seen in the red line possibly because the wings of the NeI 630.5 nm spectra leaks into the red line (630.0 nm). There is a sudden drop in the cloud-indicator brightness around 4 UTC on August 22, this is due to nearby stadium light, which was in HiT&MIS FOV, being switched off. The cloud-indicator brightness on August 22 is around the same level as August 21 even with the stadium light on, and lower after the stadium light was turned off. This suggests that the sky on August 22, 2017 (night of the TID event) was relatively cloud free near HiT&MIS's FOV.

3.2 DTEC data

To validate the wave-like brightness perturbation seen in the spectral data, DTEC maps over the continental USA were used. Figure 4 shows an example of the GPS-derived DTEC maps and a set of keograms crossing the location of the HiT&MIS instrument. Figure 4 (a, top) shows the geographical extent of the large-scale perturbations at 4:30 UTC, when the geomagnetic activity was already in the recovery phase. The LSTIDs are longitudinally uni-



173 **Figure 3.** Left column: Brightness keogram of Ne I (cloud indicator, top), green line (middle) and red line
 174 (bottom) as a function of look direction (or latitude) on the night of the eclipse (August 22). Brighter color
 175 represents higher brightness (in arbitrary units). Section 2.1 describes how the look directions are converted
 176 to latitudes. Center column: Brightness averaged over the whole field of view (0.1° by 50°) for each represen-
 177 tative keogram on the left. Notice clear wave-like perturbations seen in both red and green lines on August 22.
 178 Right column: Same as the center panel but on the night before the eclipse (August 21, keogram not shown).
 179 Note: as no photometric calibration was done and since the sensitivity of the instrument is not the same at dif-
 180 ferent spectral region, red and green brightnesses cannot be compared. That is, green line arbitrary brightness
 181 of 40 could be brighter than the red-line arbitrary brightness of 100.

192 form in longitudes west of $\sim 100^\circ\text{W}$, whereas further east they are generally latitudinally uni-
 193 form. 100°W is where approximate line of geomagnetic declination angle 0° lies, and so, the
 194 observed structures could be associated with it. Further, keograms in Figure 4b-c show the
 195 temporal extent of the LSTIDs in the meridional and zonal direction above the HIT&MIS
 196 location. The peak TID activity was observed in the time range of 3–6 UT. Figure 5 shows
 197 concurrent, co-aligned time series of DTEC and the dynamic part of the red and green line
 198 profiles obtained by polynomial de-trending at Carbondale, IL. The perturbations in the
 199 DTEC and in the green and red line brightness coincide at 3–6 UTC, which is also the time
 200 period when significant large-scale perturbations were observed in the DTEC keogram (Fig-
 201 ure 4).

3.3 Digisonde MUF data

To further verify the large scale nature of the observed TIDs, we used digisonde-derived MUF profiles from two far away locations. Figure 6 shows the MUF timelines at MH and INL from 19 UTC on August 21, 2017 to 6 UTC August 22, 2017. The MUF variability is significant at both locations. Perturbations are also seen immediately prior to the start of geomagnetic disturbances (0 UTC on August 22, 2017). These pre-midnight perturbations might be associated with the after-effect of the eclipse, as *Goncharenko et al.* [2018] also reported enhanced plasma density over MH around 21 UTC (August 21) based on radar measurements. *Goncharenko et al.* [2018] attributed these enhancements to the eclipse's aftereffect. On the other hand, the post-midnight DTEC, red and green-line brightnesses and MUF dynamics were more likely associated with the TIDs generated due to an increase in auroral currents as a result of enhanced geomagnetic activity. We expand on this further in the following section.

4 What caused the observed TIDs?

To understand the cause of the observed AGWs and TIDs, we analyzed the geomagnetic conditions. Figure 7 shows the Dst and the Auroral Electrojet (AE) indices from 18 UTC on August 21 to 10 UTC on August 22, 2017. The Dst index is a measure of the equatorial ring current strength and is obtained by averaging ground-based measurements of magnetic fields near the equator. The AE index is a measure of the strength of auroral currents and is obtained from magnetic field measurements near the polar cap. The AE strength is directly related to Joule heating of the IT system [*Eyiguler et al.*, 2018] which, in turn, could potentially lead to equatorward propagating TIDs [see *Kauristie et al.*, 2017, and references therein].

LSTIDs arrived over the FOV at about 1 UTC and lasted until around 6 UTC. Likewise, the AE index began to intensify at approximately the same time, and relaxed back to prior values after 6 UTC. In addition, the keograms showed a complex structuring of the LSTIDs. The leading fronts initially arrived from the north-east and moved towards the south-west (1–4 UTC), but were almost perfectly elongated in the zonal direction later (4–6 UTC). TIDs in smaller scales within the LSTIDs can also be observed; these are most likely caused by wave breaking of the LSTIDs. We thus conclude that the observed LSTIDs

(and AGWs) were most likely generated by geomagnetic effects that induced changes in the auroral current leading to rapid heating and expansion of the thermosphere.

5 Wave Characteristics

We performed wavelet analyses on the red and green line brightness profiles obtained at Carbondale, IL, digisonde MUF profiles obtained at INL and MH, and the DTEC measurements for Carbondale, IL. Wavelet analysis has been used by previous studies to identify wave characteristics of AGWs and TIDs [e.g., *Singh and Pallamraju*, 2016; *Kim and Chang*, 2018]. *Singh and Pallamraju* [2016] studied the vertical propagation of AGWs due to a cyclone by performing wavelet analysis on optical emission brightnesses originating at different altitudes. *Kim and Chang* [2018] used wavelet analysis to study the variation in the geomagnetic field induced by eclipses.

The wavelet analysis is based on the guide presented in *Torrence and Compo* [1998] and implemented using the Waipy package on Python (<https://github.com/mabelcalim/waipy>). Red and green line brightness profiles averaged over the whole FOV were used as there was no significant change in dynamic behavior as a function of elevation angle (or latitude, see Figure 3). The average brightnesses and MUF profiles were subtracted with a polynomial fit in order to remove the long-term climatological trends. The extraction of the dynamic part of the TEC measurement, DTEC, has been described in Section 2.2. These dynamic profiles were then zero-mean, unit variance normalized and the wavelet analysis was performed on these normalized values. Finally, the dominant time periods were obtained from the global wavelet spectra whose Full Width at Half Max (FWHM) was used to estimate the uncertainty.

The wavelet spectra for the red and the green lines, shown in Figure 8, reveal a dominant wave period of 1.2 ± 0.5 hours for the red line and 1.6 ± 0.8 hours for the green line. However, the wavelet power for the red line peaked around 2–5 UTC and the green line wavelet power peaked around 3–6 UTC. The DTEC wavelet spectra show a dominant time period of 1.7 ± 0.7 hours and also has a peak around 3–6 UTC (Figure 9). The MUF wavelet spectra for both locations show similar dominant wave periods of around 1 hour (and other modes) with peaks at two different times (within 2–6 UT, Figure 10). The wave period of 1 hour prior to midnight UTC (at MH) could be the aftereffect of the eclipse (as discussed earlier) since the perturbations precede geomagnetic disturbances.

290 The vertical phase speed (c_z) above the spectrograph was found to be 7 m/s estimated
 291 using the time delay obtained by performing cross-correlation analysis on the dynamic part
 292 of the red and green line profiles and the difference in their peak altitudes (250 km and 220
 293 km, respectively). The vertical wavelength, $\lambda_z = c_z \tau_z = 36$ km, was calculated using the aver-
 294 age of the red and the green line dominant wave time periods ($\tau_z = 1.4$ hours) and the vertical
 295 phase speed ($c_z = 7$ m/s).

296 We used maps of DTEC to estimate horizontal wave parameters. Due to a longitudi-
 297 nal structuring of the LSTIDs, we used a latitudinal keogram elongated along 120°W, shown
 298 in Figure 11a. The slope of propagation was found to be 10° per 30 minutes, which trans-
 299 lates to a meridional speed of 616 m/s, equatorward. A similar estimate was also made at
 300 Carbondale, IL, using the keogram in Figure 4. Spectral analysis [Mrak *et al.*, 2018b] was
 301 applied to the keogram in Figure 11a to obtain the dominant meridional wavenumber. The
 302 dominant meridional wavenumber is ~ 0.005 km⁻¹ which translates to meridional wavelength
 303 $\lambda_m = 1256$ km.

306 6 Effects of the Total Solar Eclipse on the observed LSTIDs

307 A total solar eclipse had occurred eight hours earlier before the observed LSTIDs (at
 308 Carbondale, IL). While the LSTIDs were most likely generated by geomagnetic effects, the
 309 effect of a total solar eclipse on the IT system has also been well-documented by recent and
 310 prior studies [e.g., Coster *et al.*, 2017; Mrak *et al.*, 2018a; Liu *et al.*, 1998]. Furthermore,
 311 the MUF profile at MH showed perturbations even prior to the start of the geomagnetically
 312 active time (Figure 6). This could potentially be due to the lingering effect of the eclipse.

313 To test the eclipse's effect for our observations, the Global Ionosphere Thermosphere
 314 Model (GITM; Ridley *et al.* [2006]) was used to simulate the effects of the August 21, 2017
 315 eclipse on the IT system. The Flare Irradiance Spectral Model (FISM; Chamberlin *et al.*
 316 [2007]) was used to specify the solar EUV spectrum, but this was modified to reduce the
 317 EUV heating and ionization in the region of the lunar occultation of the Earth to simulate the
 318 eclipse effect. This was done as described by Wu *et al.* [2018], although they used a different
 319 EUV model. The path of the eclipse was defined in Geocentric Solar Ecliptic (GSE) coordi-
 320 nates as a straight line in the (Y_{GSE}, Z_{GSE})-plane, assuming X_{GSE} constant. The reduction
 321 in EUV irradiance was based on the distance between each GITM grid point and the center
 322 of totality; at the center of totality, the EUV irradiance was reduced to 10% of the normal

323 value, which linearly increased until the edge of the occultation region was approached, after
324 which the EUV increased exponentially back to 100% at 3,800 km distance from the center
325 of totality.

333 Four simulations were performed. First, a set of two simulations was run with observed
334 IMF and solar wind data to drive the high-latitude electric potential and auroral precipitation
335 patterns. One of these simulations included the effects of the eclipse, while the other (the
336 control run) did not. To test the influence of variable geomagnetic activity on the results, an
337 additional set of simulations (eclipse and control) were run with actual solar wind conditions
338 and constant IMF, i.e., fixed geomagnetic activity. For these two simulations with constant
339 IMF, the following solar wind and IMF parameters were used: solar wind speed = 534 km/s,
340 solar wind density = 4.0 cm^{-3} , $B_x = -3.1 \text{ nT}$, $B_y = -2.3 \text{ nT}$, and $B_z = -3.0 \text{ nT}$. All the simula-
341 tions were otherwise set up identically. The model was run with a resolution of 2.0° in lati-
342 tude, 4.0° in longitude, and ~ 0.3 times the scale height in altitude, spanning from 100 km to
343 approximately 600 km altitude. The simulations with observed solar wind and IMF param-
344 eters used here are the same as those analyzed by Cnossen et al. [in review], who describe the
345 simulation setup in further detail.

346 Figure 12 shows the electron density, the thermospheric O/N₂ ratios, and plasma and
347 neutral temperatures estimated using GITM at 250 km, which is where the red line emis-
348 sion peaks, for the four cases: with and without the effect of the eclipse for actual and con-
349 stant geomagnetic activity. The electron density and the O/N₂ ratio were around 10% higher
350 when the the eclipse's effect were included but the time profile was very similar to the non-
351 eclipse case for both geomagnetic activity conditions. All the temperatures are slightly lower
352 (compared to density changes) when the eclipse's effect is considered. For actual geomag-
353 netic activity conditions, there is a slight enhancement in the electron density between 1–
354 2 UT, but no wave-like perturbation is seen. While the results imply that the IT system is
355 pre-conditioned even hours after the eclipse event, no LSTIDs are observed with the sim-
356 ulations for any of the selected conditions. We thus conclude that there is no evidence that
357 the eclipse had any effect on the observed LSTIDs, although we cannot completely rule out
358 such effects, since the model did not reproduce the observed LSTIDs for any of the simulated
359 cases.

7 Discussion

Wave-like structures were observed in red and green line emissions and GPS TEC measurements at Carbondale, IL as well as in digisonde measurements at Idaho National Laboratory and Millstone Hill. These observations showed that the dynamic part of the red and green lines and the DTEC profiles at Carbondale, IL, coincided best around 3–6 UTC (August 22, 2017, Figure 5), which is also when the DTEC keogram show prominent LSTIDs (Figure 4, bottom). All of the wavelet spectra also have a similar dominant wave power around the same time frame (3–6 UTC). In addition, the AE index peaks and recovers during the same time period too (Figure 7). This indicates that the increase in auroral currents and associated Joule heating near the poles were responsible for the observed LSTIDs. There are TIDs prior to and after 3–6 UTC in the DTEC map (Figure 4, bottom); however, their scale sizes are smaller and they are weaker.

Multi-spectral observation from HiT&MIS would have been sufficient to infer the vertical wave characteristics of the TID. However, the brightness perturbation spanned its FOV, so the meridional scale-size of the TID could not have been estimated. Similarly, using the DTEC measurements, meridional wave characteristics could have been estimated, but not the vertical wave characteristics. Thus, by using multiple measurements in combination we were able to do a more comprehensive analysis of the wave properties than would have been possible with individual measurements in isolation.

The estimated dominant wave time-periods are slightly different for different observations, i.e., 1.2 ± 0.5 , 1.6 ± 0.8 and 1.7 ± 0.7 h for the red line, green line and DTEC, respectively at Carbondale, IL. The dominant wave period of around 1h was also found for MUF profiles at both INL and MH. MUF is sensitive to the bottom-side ionospheric plasma densities, the red and green line brightnesses are sensitive to both the plasma and the neutral densities at the altitude they peak at, and the TEC measurements are sensitive to the line of sight ionospheric plasma density. These differences could explain the minor discrepancy in dominant time periods.

Previous studies have observed disturbances in the IT system well after the eclipse and far away from its path [e.g, *Harding et al.*, 2018; *Verhulst and Stankov*, 2018]. *Goncharenko et al.* [2018] reported enhanced electron density (> 50-150%) starting from 21 UTC, August 21, 2017 to at least midnight UTC (August 22) based on radar measurements at MH hours after the eclipse. The authors attributed this enhancement in electron density to the down-

ward flux of plasma from the plasmasphere that was initially filled by upwelling of plasma immediately following the eclipse. This electron density enhancement was not predicted by GITM, as it does not include contributions from the plasmasphere. 21–22 UTC is also when one of the peaks in the MUF wavelet spectrum with a dominant wave time-period of around 1h at MH is observed (Figure 10). This indicates that the observed perturbation in MUF was caused by an eclipse-related effect with a similar time period of around 1h as was observed later, probably in relation to geomagnetic disturbance effects. *Wu et al.* [2018] reported that the IT system's response to the eclipse in GITM decays much quicker than is seen in TEC and NmF2 observations. On the other hand, a 10% increase in both O/N₂ ratio and N_e at Carbondale, IL predicted by GITM is consistent with the quantitative enhancement in red line brightness we observed when compared to the night before (see Supplementary Figure 2). However, GITM failed to produce the wave-like perturbations seen in red and green line airglow brightnesses, possibly due to coarser resolution in latitude and longitude. Thus, it is possible that the eclipse's long-term effect not only influenced the TID strength, but also could have interacted with the geomagnetic effects in the formation of the observed LSTIDs. However, based on this study we could only conclude that while the eclipse effect were still present during the LSTID events, they had no detectable impact on the observed LSTIDs.

8 Summary

We have presented an analysis of wave-like perturbations observed in red and green line brightness from ground-based optical measurements. Additional insight was provided by MUF profiles based on digisonde measurements and GPS-based TEC measurements. We conclude that a geomagnetic disturbance starting at midnight UTC on August 22, 2017 enhanced the auroral currents that lead to Joule heating which triggered AGWs and associated LSTIDs propagating towards the equator. Furthermore, a total solar eclipse had occurred hours earlier over the continental USA (8 hours earlier in Carbondale, IL). By using the GITM simulations, we found that preconditioning of the IT system due to eclipse increased N_e and the O/N₂ ratio at 250 km around 10% during the observed TID event but does not seem to effect the LSTIDs. Wavelet analysis performed on all the measurements show a similar dominant time period of about 1.5 hours. Using cross-correlation analysis on the red and the green line brightness profiles, the vertical phase speed was found to be 7 m/s, corresponding to a vertical wavelength of 36 km. Similarly, spectral analysis of DTEC keogram

423 was used to estimate the meridional phase speed of 616 m/s, corresponding to a meridional
424 wavelength of 1256 km.

425 **Acknowledgments**

426 This work was partially supported by the NSF grant AGS1145166 and UMass Low-
427 ell internal funds. Sebastijan Mrak was supported by NSF grant AGS-1743832 to Boston
428 University. Dr. Ingrid Cnossen was supported by NSF grant ATM1452097. She can be con-
429 tacted for any GITM runs. GITM simulations were performed on the NASA Pleiades high
430 performance computing facilities. The brightness data from HiT&MIS used for this work
431 are available online at [10.5281/zenodo.1494258](https://doi.org/10.5281/zenodo.1494258). Digisonde data were retrieved from on-
432 line DIDBase repository of the Global Ionosphere Radio Observatory (GIRO) via its SAO
433 Explorer workstations and <http://giro.uml.edu> portal. Digisonde data from Idaho Na-
434 tional Laboratory are courtesy of Dr. James R. Hanneman. We thank Dr. Stan Solomon at
435 UCAR/NCAR for constructive discussions on the GLOW model whose Python wrapped ver-
436 sion can be found at github.com/scivision/glowaurora.

437 **References**

- 438 Altadill, D., A. Belehaki, E. Blanch, C. Borries, D. Buresova, I. Galkin, H. Haralambous,
439 J. Zornoza, J. Miguel, I. Kutiev, C. Oikonomou, J. Sanz Subirana, and I. Tsagouri (2018),
440 Report on tid algorithms.
- 441 Aryal, S., S. C. Finn, K. Hewawasam, R. Maguire, G. Geddes, T. Cook, J. Martel, J. L.
442 Baumgardner, and S. Chakrabarti (2018), Derivation of the Energy and Flux Morphology
443 in an Aurora Observed at Midlatitude Using Multispectral Imaging, *Journal of Geophysi-
444 cal Research: Space Physics*, *123*(5), 4257–4271.
- 445 Azeem, I., J. Yue, L. Hoffmann, S. D. Miller, W. C. Straka, and G. Crowley (2015), Multi-
446 sensor profiling of a concentric gravity wave event propagating from the troposphere to the
447 ionosphere, *Geophysical research letters*, *42*(19), 7874–7880.
- 448 Bailey, S. M., C. A. Barth, and S. C. Solomon (2002), A model of nitric oxide in the lower
449 thermosphere, *Journal of Geophysical Research: Space Physics*, *107*(A8).
- 450 Chakrabarti, S., O.-P. Jokiahho, J. Baumgardner, T. Cook, J. Martel, and M. Galand (2012),
451 High-throughput and multislit imaging spectrograph for extended sources, *Optical Engi-
452 neering*, *51*(1), 013,003–1, doi:10.1117/1.OE.51.1.013003.

- 453 Chamberlin, P. C., T. N. Woods, and F. G. Eparvier (2007), Flare irradiance spectral model
454 (FISM): Daily component algorithms and results, *Space Weather*, 5(7), n/a–n/a, doi:10.
455 1029/2007sw000316.
- 456 Chimonas, G., and C. Hines (1970a), Atmospheric gravity waves induced by a solar eclipse,
457 *Journal of Geophysical Research*, 75(4), 875–875.
- 458 Chimonas, G., and C. O. Hines (1970b), Atmospheric gravity waves launched by auroral cur-
459 rents, *Planetary and Space Science*, 18(4), 565–582, doi:10.1016/0032-0633(70)90132-7.
- 460 Coster, A., D. Herne, P. Erickson, and D. Oberoi (2012), Using the Murchison Widefield
461 Array to observe midlatitude space weather, *Radio Science*, 47(06), 1–8.
- 462 Coster, A. J., E. M. Gaposchkin, and L. E. Thornton (1992), Real-time ionospheric monitor-
463 ing system using GPS, *Navigation*, 39(2), 191–204.
- 464 Coster, A. J., L. Goncharenko, S.-R. Zhang, P. J. Erickson, W. Rideout, and J. Vierinen
465 (2017), GNSS Observations of Ionospheric Variations During the 21 August 2017
466 Solar Eclipse, *Geophysical Research Letters*, 44(24), 12,041–12,048, doi:10.1002/
467 2017GL075774.
- 468 Davies, K. (1989), Ionospheric radio (ionospheric radio wave propagation), *Peter Peregrinus*,
469 *Boulder, Colo.*
- 470 Davis, M. J. (1971), On polar substorms as the source of large-scale traveling ionospheric
471 disturbances, *Journal of Geophysical Research*, 76(19), 4525–4533, doi:10.1029/
472 JA076i019p04525.
- 473 Eyiguler, E. C. K., Z. Kaymaz, N. A. Frissell, J. M. Ruohoniemi, and L. RastÄdter (2018),
474 Investigating Upper Atmospheric Joule Heating Using Cross-Combination of Data for Two
475 Moderate Substorm Cases, *Space Weather*, 0(0), doi:10.1029/2018SW001956.
- 476 Goncharenko, L. P., P. J. Erickson, S.-R. Zhang, I. Galkin, A. J. Coster, and O. F. Jonah
477 (2018), Ionospheric Response to the Solar Eclipse of 21 August 2017 in Millstone Hill
478 (42n) Observations, *Geophysical Research Letters*, 0(0), doi:10.1029/2018GL077334.
- 479 Habarulema, J. B., E. Yizengaw, Z. T. KatamziJoseph, M. B. Moldwin, and S. Buchert
480 (2018), Storm Time Global Observations of Large-Scale TIDs From Ground-Based and
481 In Situ Satellite Measurements, *Journal of Geophysical Research: Space Physics*, 123(1),
482 711–724, doi:10.1002/2017JA024510.
- 483 Harding, B. J., D. P. Drob, R. A. Buriti, and J. J. Makela (2018), Nightside Detection of a
484 Large-Scale Thermospheric Wave Generated by a Solar Eclipse, *Geophysical Research
485 Letters*, 45(8), 3366–3373, doi:10.1002/2018GL077015.

- 486 Hines, C. O. (1960), Internal Atmospheric Gravity Waves at Ionospheric Heights, *Canadian*
487 *Journal of Physics*, 38(11), 1441–1481, doi:10.1139/p60-150.
- 488 Hocke, K., K. Schlegel, et al. (1996), A review of atmospheric gravity waves and travelling
489 ionospheric disturbances: 1982–1995, *Annales Geophysicae*, 14(9), 917.
- 490 Kauristie, K., A. Morschhauser, N. Olsen, C. C. Finlay, R. L. McPherron, J. W. Gjerloev,
491 and H. J. Opgenoorth (2017), On the Usage of Geomagnetic Indices for Data Selec-
492 tion in Internal Field Modelling, *Space Science Reviews*, 206(1), 61–90, doi:10.1007/
493 s11214-016-0301-0.
- 494 Kelley, M. C. (2011), On the origin of mesoscale TIDs at midlatitudes., *Annales Geophysi-*
495 *cae (09927689)*, 29(2).
- 496 Kim, J.-H., and H.-Y. Chang (2018), Geomagnetic field variations observed by INTERMAG-
497 NET during 4 total solar eclipses, *Journal of Atmospheric and Solar-Terrestrial Physics*,
498 172, 107–116, doi:10.1016/j.jastp.2018.03.023.
- 499 Klobuchar, J. A. (1987), Ionospheric time-delay algorithm for single-frequency GPS users,
500 *Tech. rep.*, AIR FORCE SYSTEMS COMMAND HANSCOM AFB MA GEOPHYSICS
501 LAB.
- 502 Lin, C. Y., Y. Deng, and A. Ridley (2018), Atmospheric Gravity Waves in the Ionosphere and
503 Thermosphere During the 2017 Solar Eclipse, *Geophysical Research Letters*.
- 504 Liu, J. Y., C. C. Hsiao, L. C. Tsai, C. H. Liu, F. S. Kuo, H. Y. Lue, and C. M. Huang (1998),
505 Vertical phase and group velocities of internal gravity waves derived from ionograms dur-
506 ing the solareclipse of 24 October 1995, *Journal of Atmospheric and Solar-Terrestrial*
507 *Physics*, 60(17), 1679–1686, doi:10.1016/S1364-6826(98)00103-5.
- 508 Lowell Digisonde International, L. (2018), Digisonde DPS4D Manual.
- 509 Mrak, S., J. Semeter, D. Drob, and J. D. Huba (2018a), Direct EUV/X-Ray Modulation of
510 the Ionosphere During the August 2017 Total Solar Eclipse, *Geophysical Research Letters*,
511 45(9), 3820–3828, doi:10.1029/2017GL076771.
- 512 Mrak, S., J. Semeter, Y. Nishimura, M. Hirsch, and N. Sivadas (2018b), Coincidental TID
513 Production by Tropospheric Weather During the August 2017 Total Solar Eclipse, *Geo-*
514 *physical Research Letters*, doi:10.1029/2018GL080239.
- 515 Munro, G. (1950), Travelling disturbances in the ionosphere, *Proc. R. Soc. Lond. A*,
516 202(1069), 208–223.
- 517 Pröls, G. W., and M. Očko (2000), Propagation of upper atmospheric storm effects to-
518 wards lower latitudes, *Advances in Space Research*, 26(1), 131–135, doi:10.1016/

519 S0273-1177(99)01039-X.

520 Reinisch, B. W., and I. A. Galkin (2011), Global ionospheric radio observatory (giro), *Earth,*
521 *planets and space*, 63(4), 377–381.

522 Reinisch, B. W., I. A. Galkin, G. Khmyrov, A. Kozlov, K. Bibl, I. Lisysyan, G. Cheney,
523 X. Huang, D. Kitrosser, V. Paznukhov, et al. (2009), New digisonde for research and moni-
524 toring applications, *Radio Science*, 44(1).

525 Ridley, A. J., Y. Deng, and G. Toth (2006), The global ionosphere–thermosphere model,
526 *Journal of Atmospheric and Solar Terrestrial Physics*, 68(8), 839–864.

527 Singh, R. P., and D. Pallamraju (2016), Effect of cyclone Nilofar on mesospheric wave dy-
528 namics as inferred from optical nightglow observations from Mount Abu, India, *Journal of*
529 *Geophysical Research: Space Physics*, 121(6), 5856–5867, doi:10.1002/2016JA022412.

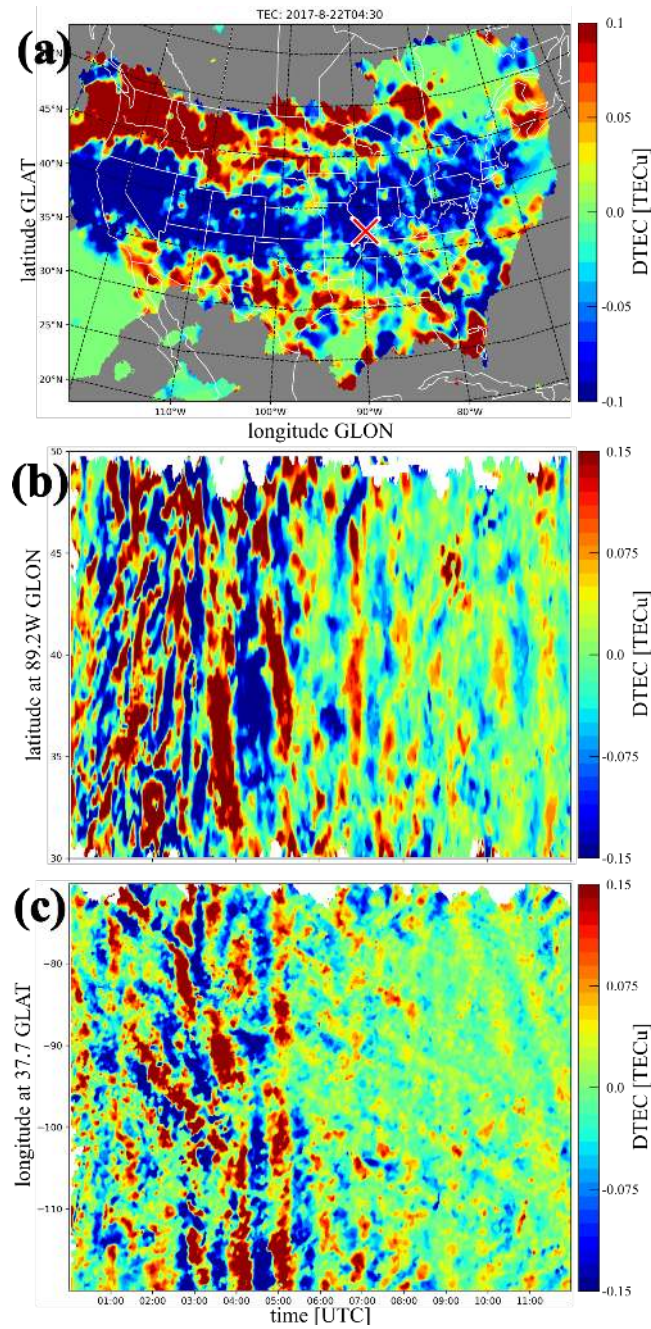
530 Solomon, S. C., and V. J. Abreu (1989), The 630 nm dayglow, *Journal of Geophysical Re-*
531 *search: Space Physics*, 94(A6), 6817–6824.

532 Solomon, S. C., P. B. Hays, and V. J. Abreu (1988), The auroral 6300 Å emission: Obser-
533 vations and modeling, *Journal of Geophysical Research: Space Physics*, 93(A9), 9867–
534 9882, doi:10.1029/JA093iA09p09867.

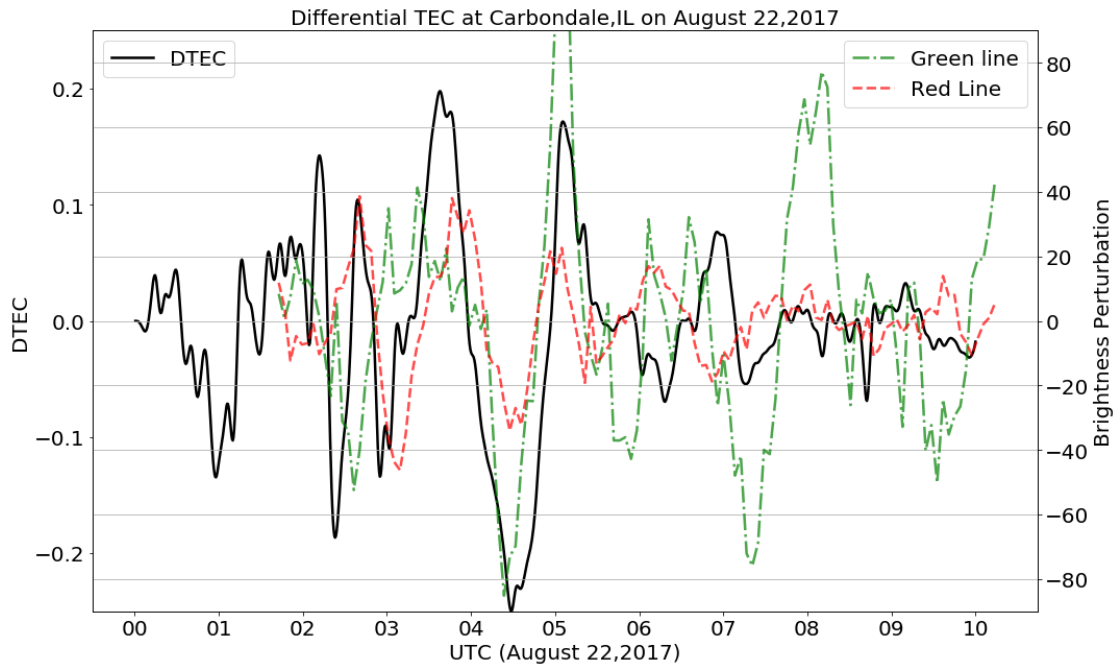
535 Torrence, C., and G. P. Compo (1998), A practical guide to wavelet analysis, *Bulletin of the*
536 *American Meteorological society*, 79(1), 61–78.

537 Verhulst, T. G., and S. M. Stankov (2018), Ionospheric wave signature of the American solar
538 eclipse on 21 August 2017 in Europe, *Advances in Space Research*, 61(9), 2245–2251.

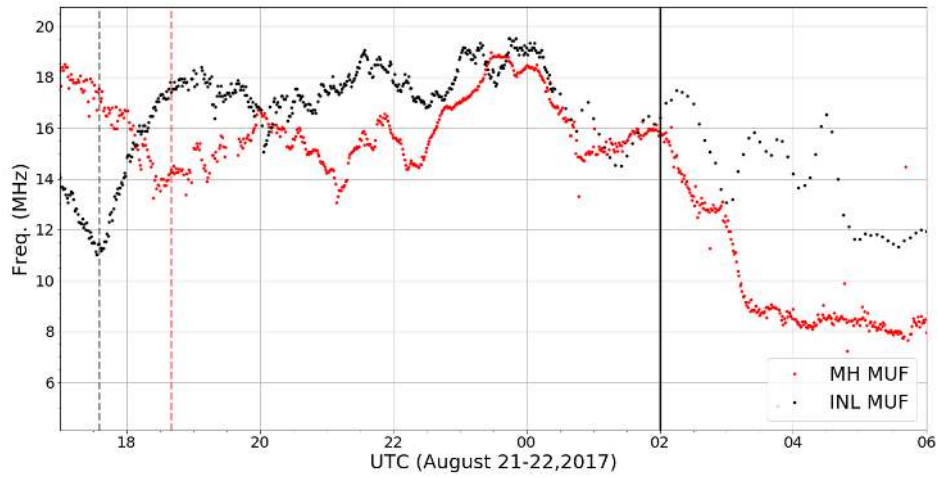
539 Wu, C., A. J. Ridley, L. Goncharenko, and G. Chen (2018), GITM-Data Comparisons of the
540 Depletion and Enhancement During the 2017 Solar Eclipse, *Geophysical Research Letters*,
541 45(8), 3319–3327.



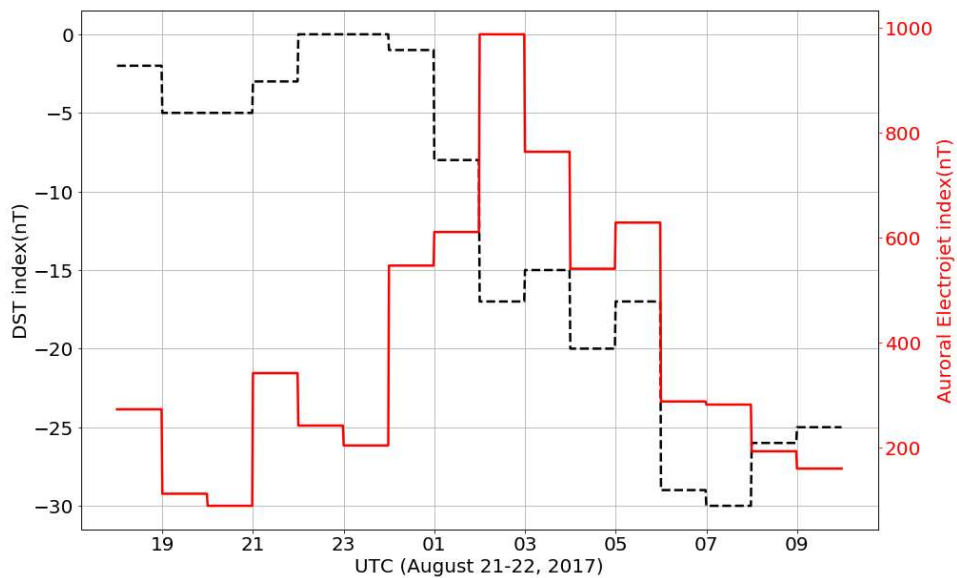
183 **Figure 4.** The LSTIDs event as observed by GPS-aided DTEC maps. (a, top) A representative GPS map of
 184 TIDs over continental US at 4:30 UTC. The red 'X' mark denotes the location of the HiT&MIS instrument
 185 at Carbondale, IL (37.7°N , 89.2°W). (b, middle) A DTEC keogram elongated along 89.2°W longitude. (c,
 186 bottom) A DTEC keogram elongated along 37.7°N latitude.



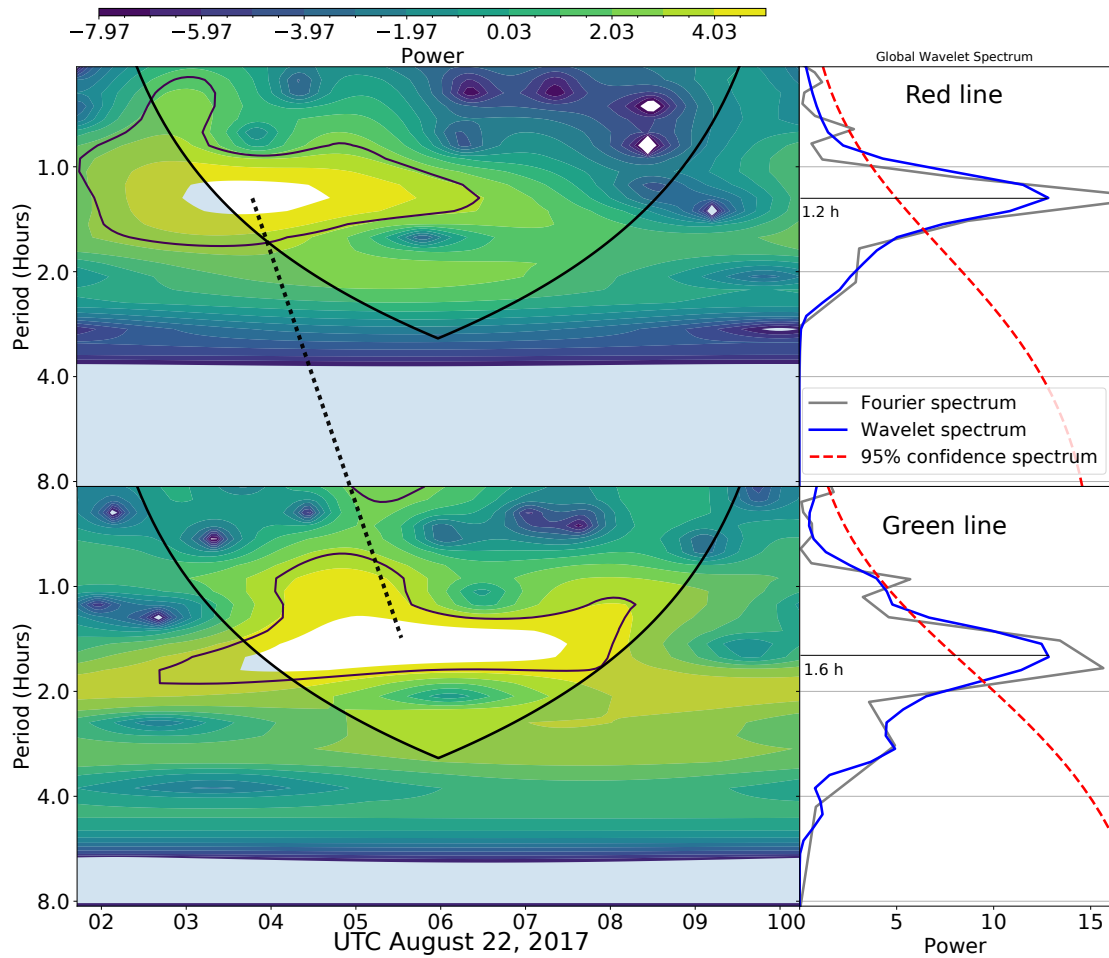
202 **Figure 5.** DTEC obtained for Carbondale, IL on August 22, 2017 from GPS-derived TEC measurements
 203 (solid black lines). Notice stronger perturbations and better coincidence from 3–6 UTC (compared to the
 204 whole profile) with red and the green line profiles shown in dot-dashed and dashed lines, respectively. This
 205 time-frame also coincides with the stronger large-scale DTEC perturbation (Figure 4) and peak enhancement
 206 and recovery of the AE index (Figure 7).



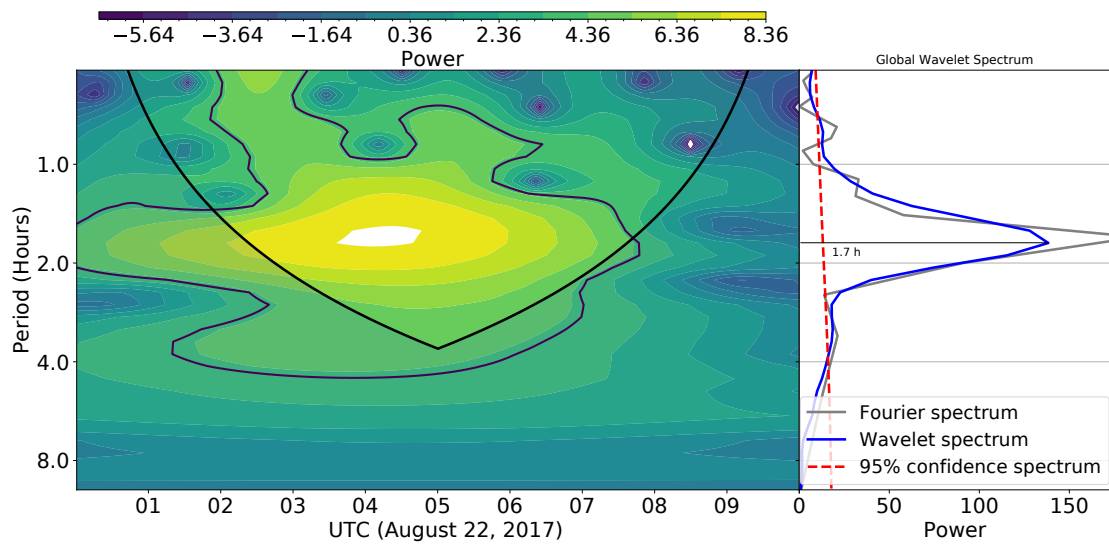
220 **Figure 6.** Digisonde-derived MUF profiles at Idaho National Lab (INL) and Millstone Hill (MH) from
 221 17 UTC August 21 to 6 UTC August 22, 2017. INL was close to the path of the totality and the 99% peak ob-
 222 scuration time is shown by the dashed vertical black line. MH was on the path of partial eclipse and the 60%
 223 peak obscuration time is shown by the dashed vertical red line. HiT&MIS observation starts around 2 UTC on
 224 August 22, indicated by the vertical solid black line.



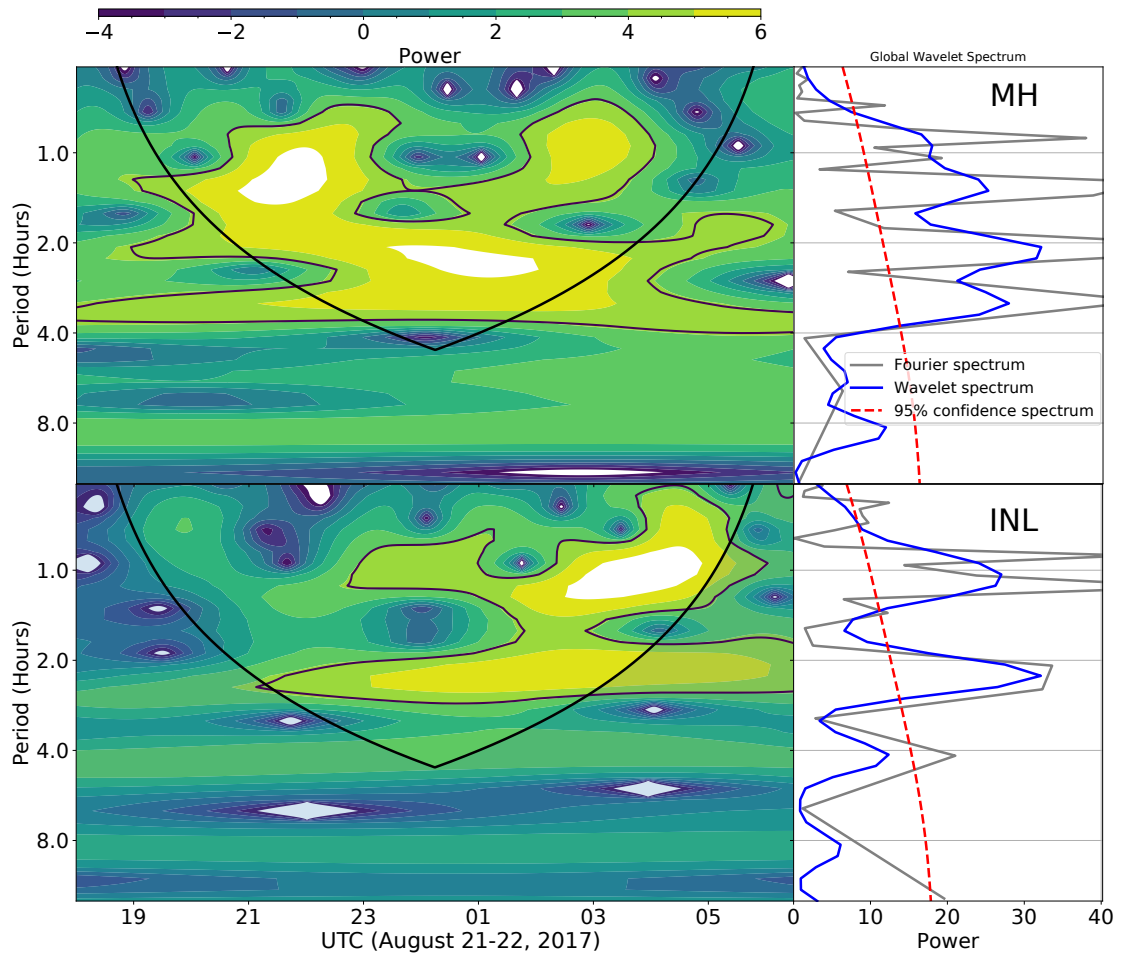
244 **Figure 7.** Dst and AE indices before and during HiT&MIS observation times. Note the increase in AE
 245 starting at midnight UTC on August 22, 2017.



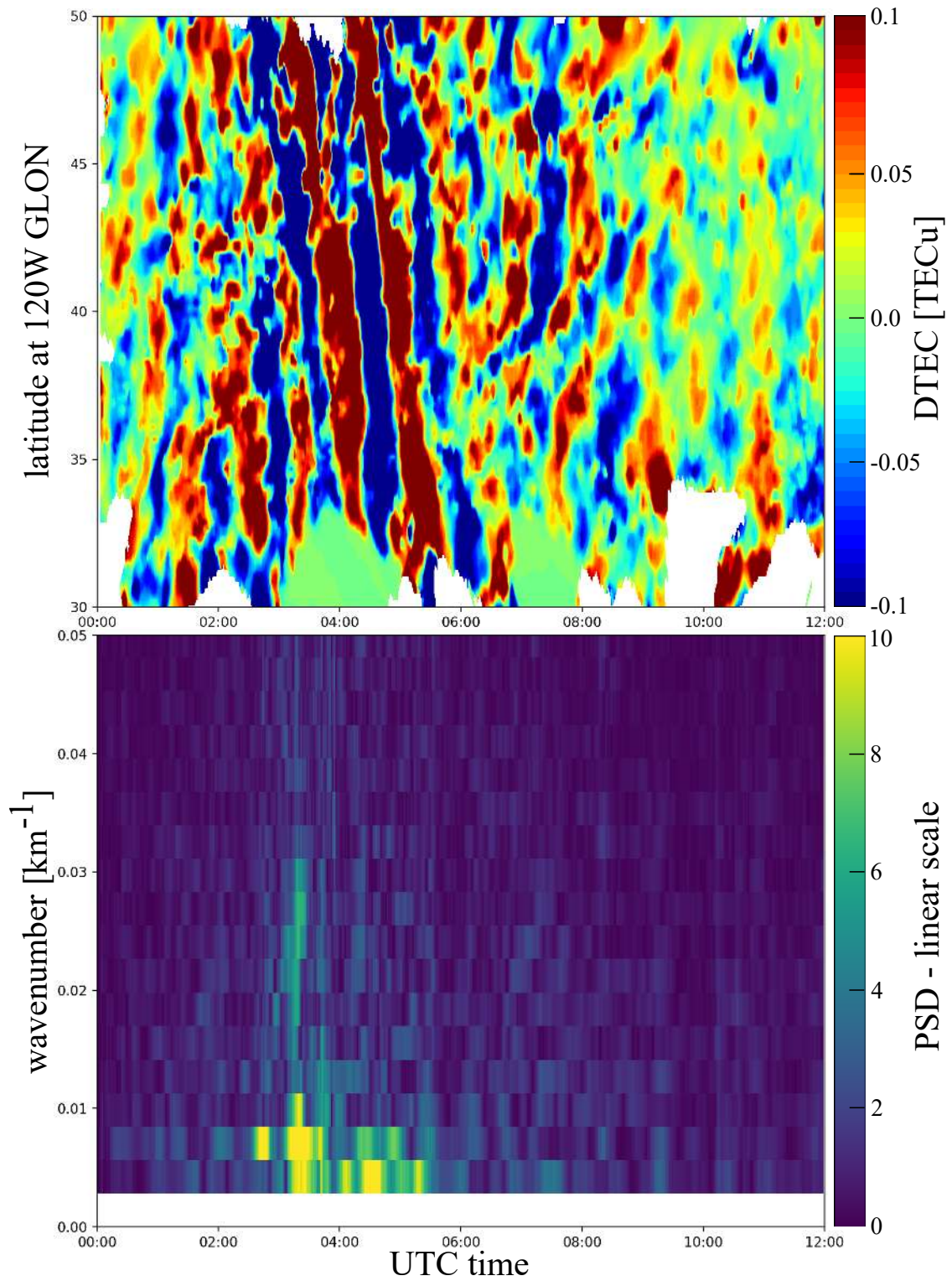
275 **Figure 8.** Left: Wavelet analyses performed on the de-trended red and green line brightnesses. A dominant
 276 wave period of 1.2 hour and 1.6 hour was found for the red and the green lines, respectively. A dashed-black
 277 line is shown to highlight the shift in peak time-periods from the red to the green line. The parabolic black
 278 line represents the cone of influence, below which the results are unreliable. The 95% confidence-level pow-
 279 ers on the wavelet spectra are represented by the dark-purple contour. Right: The wavelet power spectrum
 280 averaged along all observation times and the corresponding Fast Fourier Transform (FFT) power spectrum
 281 and wavelet spectrum are shown in gray and black, respectively. The 95% confidence interval for the global
 282 spectra are shown in red.



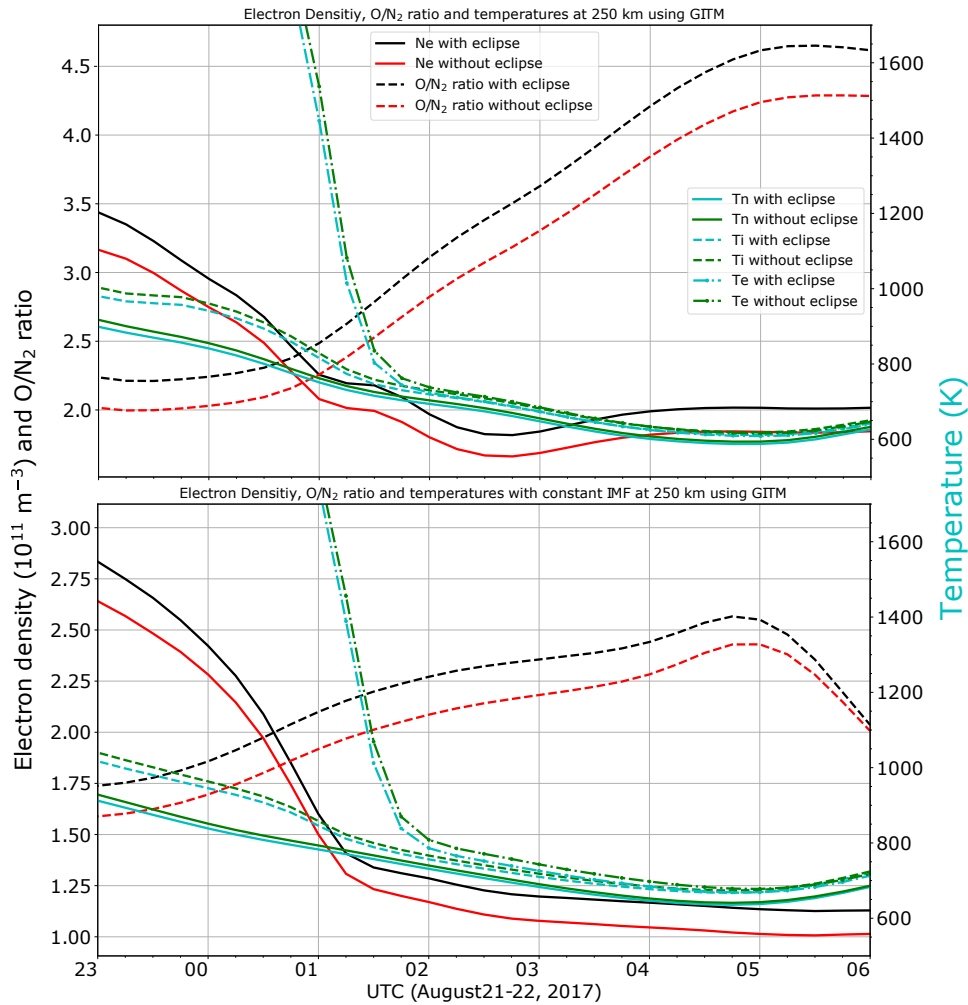
283 **Figure 9.** Wavelet analysis performed on the DTEC profile at Carbondale, IL from GPS TEC measure-
284 ments. The dominant time period of 1.7 hour is seen starting around 4 UTC.



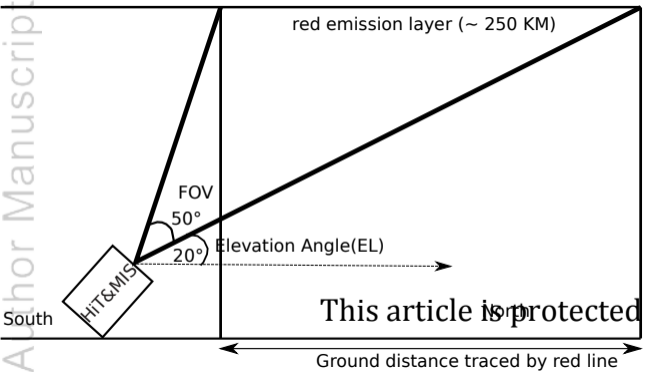
285 **Figure 10.** Left: Wavelet analysis performed on the dynamic part of the MUF profiles from the MH (top)
 286 and INL (bottom). A dominant time period of 1 hour is seen at both locations at different times after midnight
 287 UTC is most likely associated with the enhancement in AE. Notice wavelet power spectrum with a dominant
 288 time period of 1 hour starting around 21 UTC at Millstone Hill which is before the commencement of the
 289 minor geomagnetic storm and could be associated with the after-effect of the eclipse.

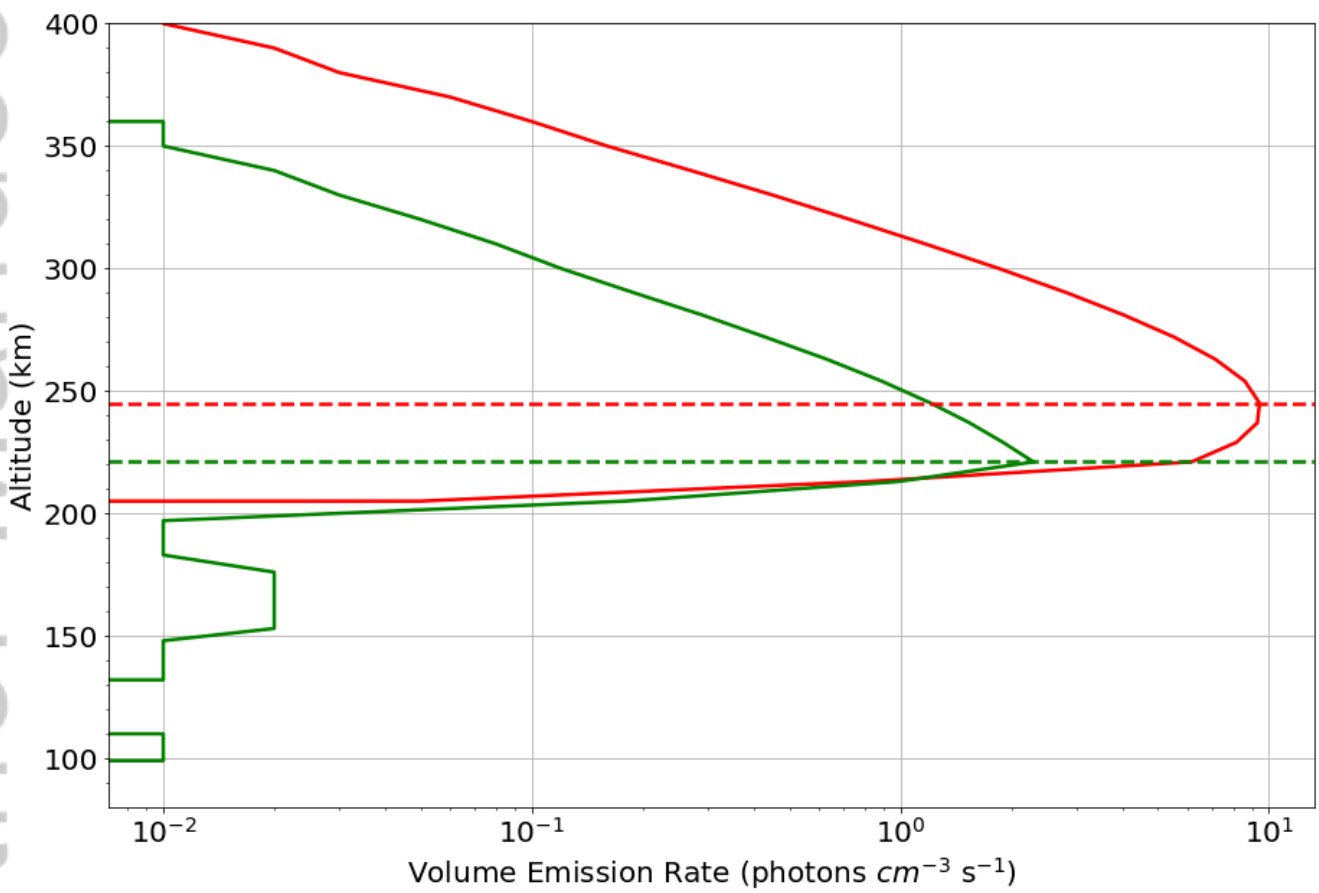


304 **Figure 11.** LSTID analysis of meridional propagation velocity at 120°W (a), and meridional wavelength
305 utilizing 2D FFT analysis (b).

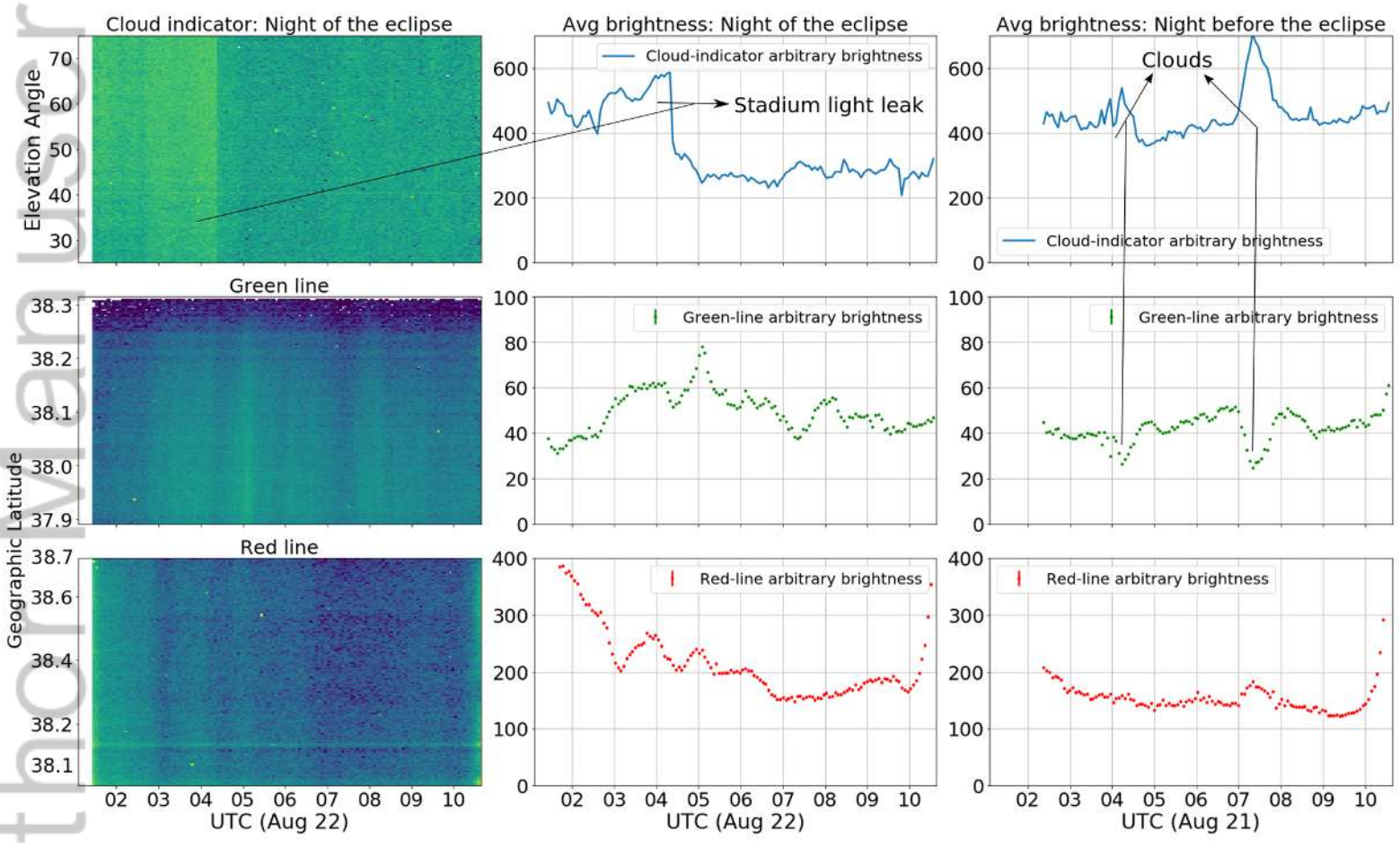


326 **Figure 12.** Electron densities (Ne), thermospheric O/N₂ ratio, and plasma and neutral temperatures at 250
 327 km (peak of red line emission) as modeled by GITM for the eclipse and non-eclipse (control) conditions with
 328 actual geomagnetic conditions (top) and constant geomagnetic conditions (bottom) at Carbondale, IL. While
 329 the profiles are very similar, electron density and the O/N₂ ratios are ~ 10% higher when the effects due the
 330 eclipse were included (for both actual and constant geomagnetic activity). All the temperatures (Tn: neutral
 331 temperature, Ti: ion temperature, Te: electron temperature) are slightly lower when the eclipse's effect is
 332 included.

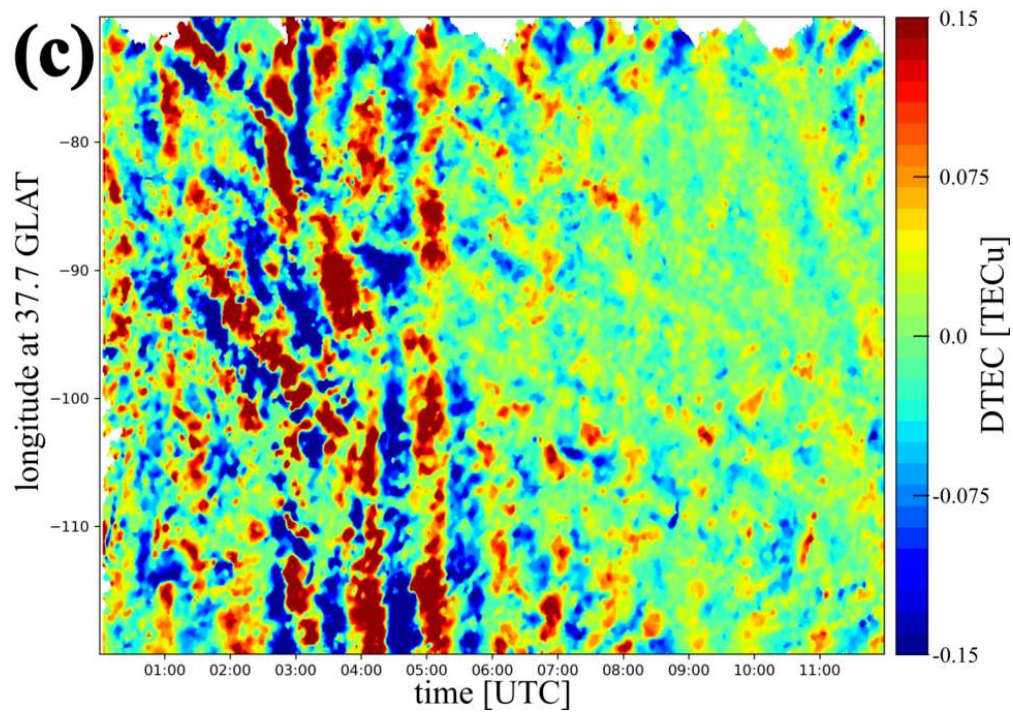
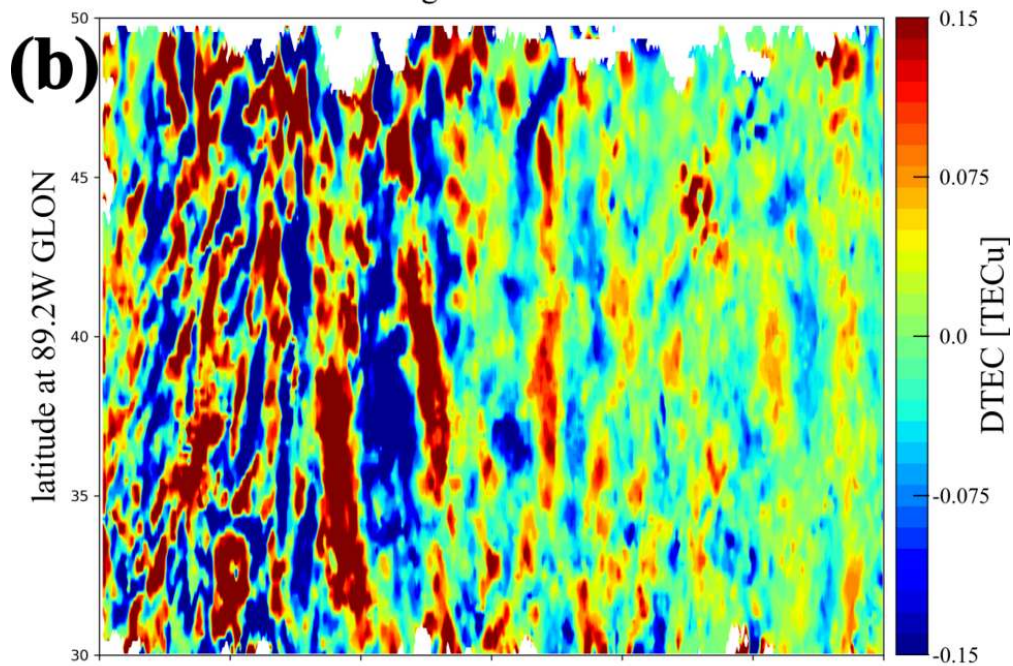
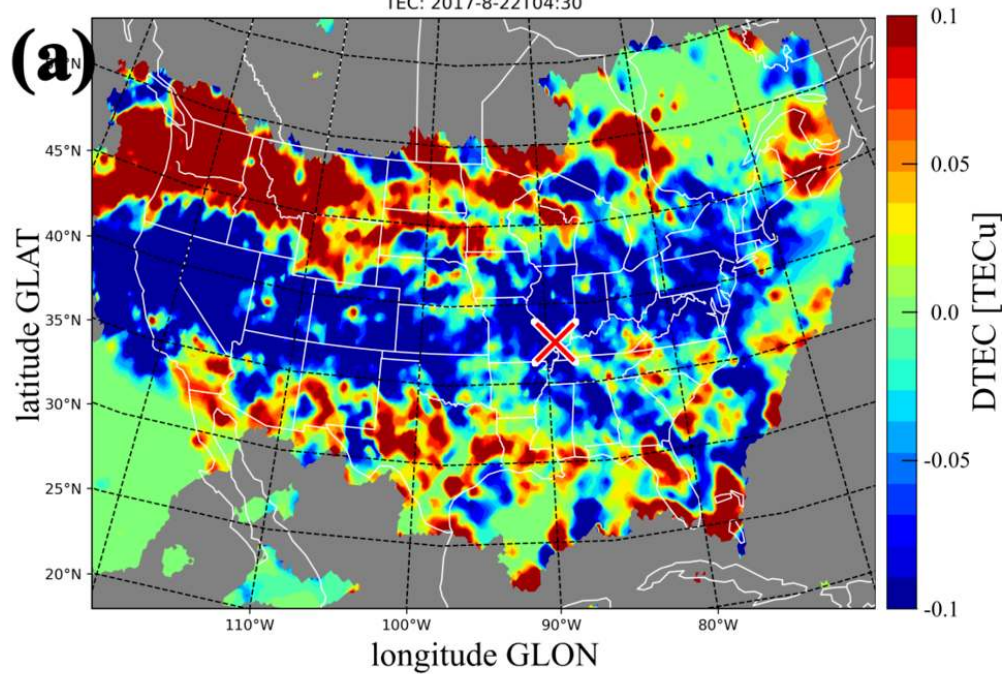




2018JA026333-f02-z-.png

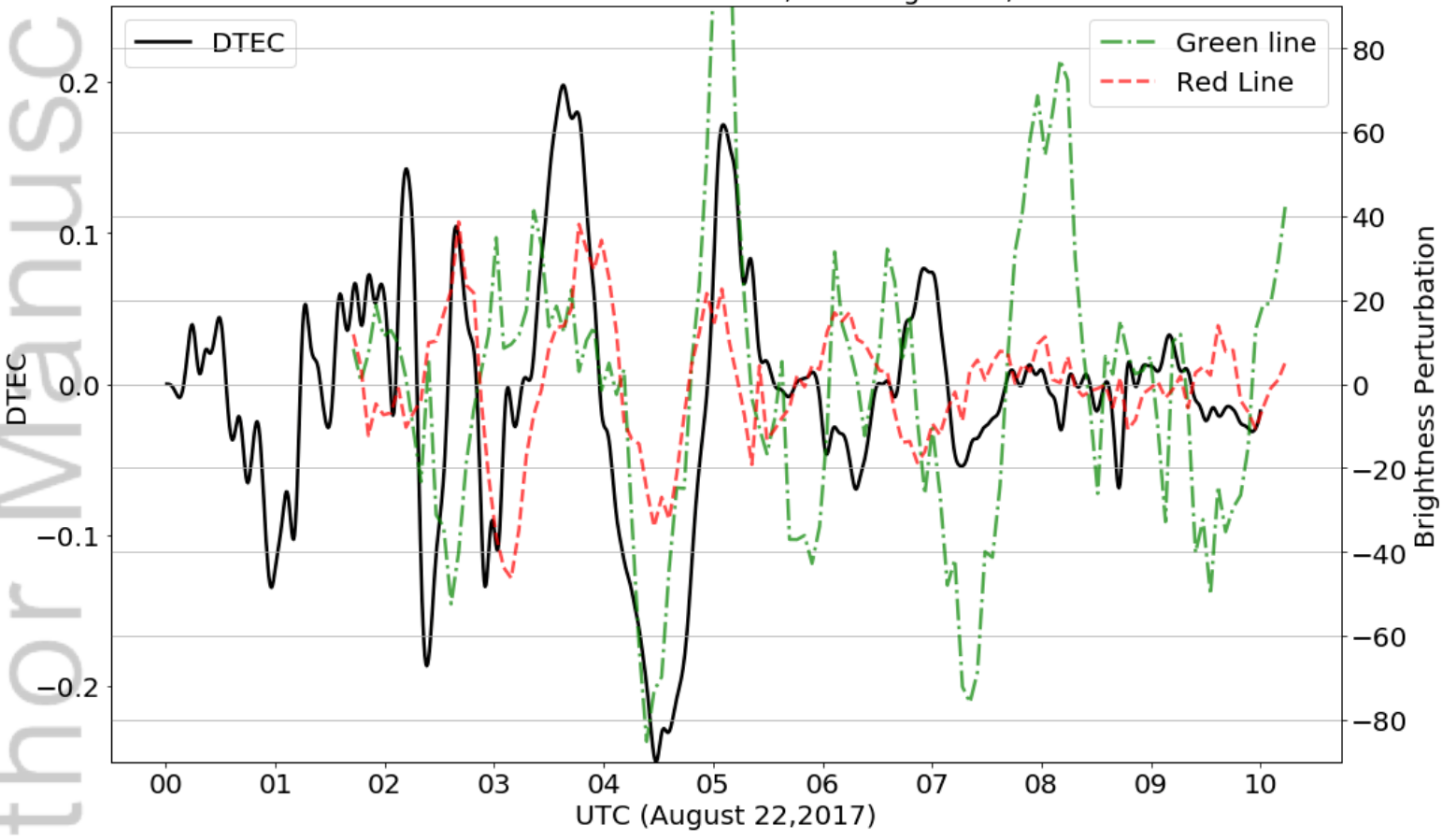


2018JA026333-f03-z-.png

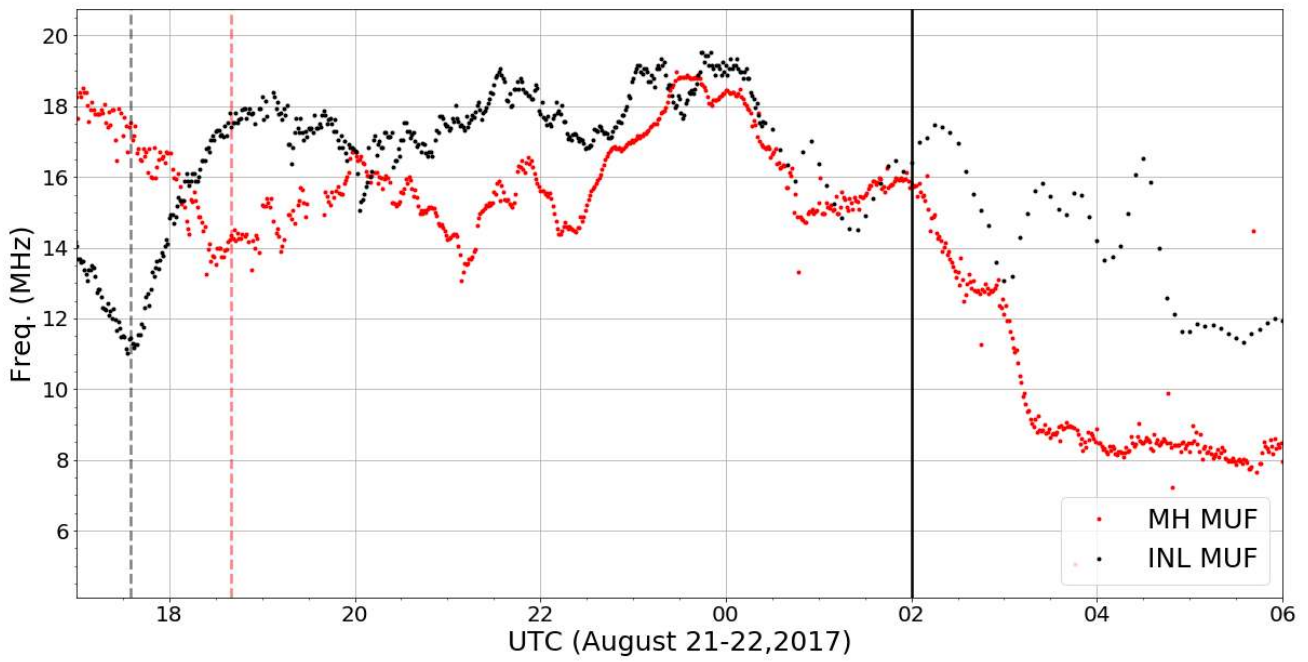


2018JA026333-f04-z-.png

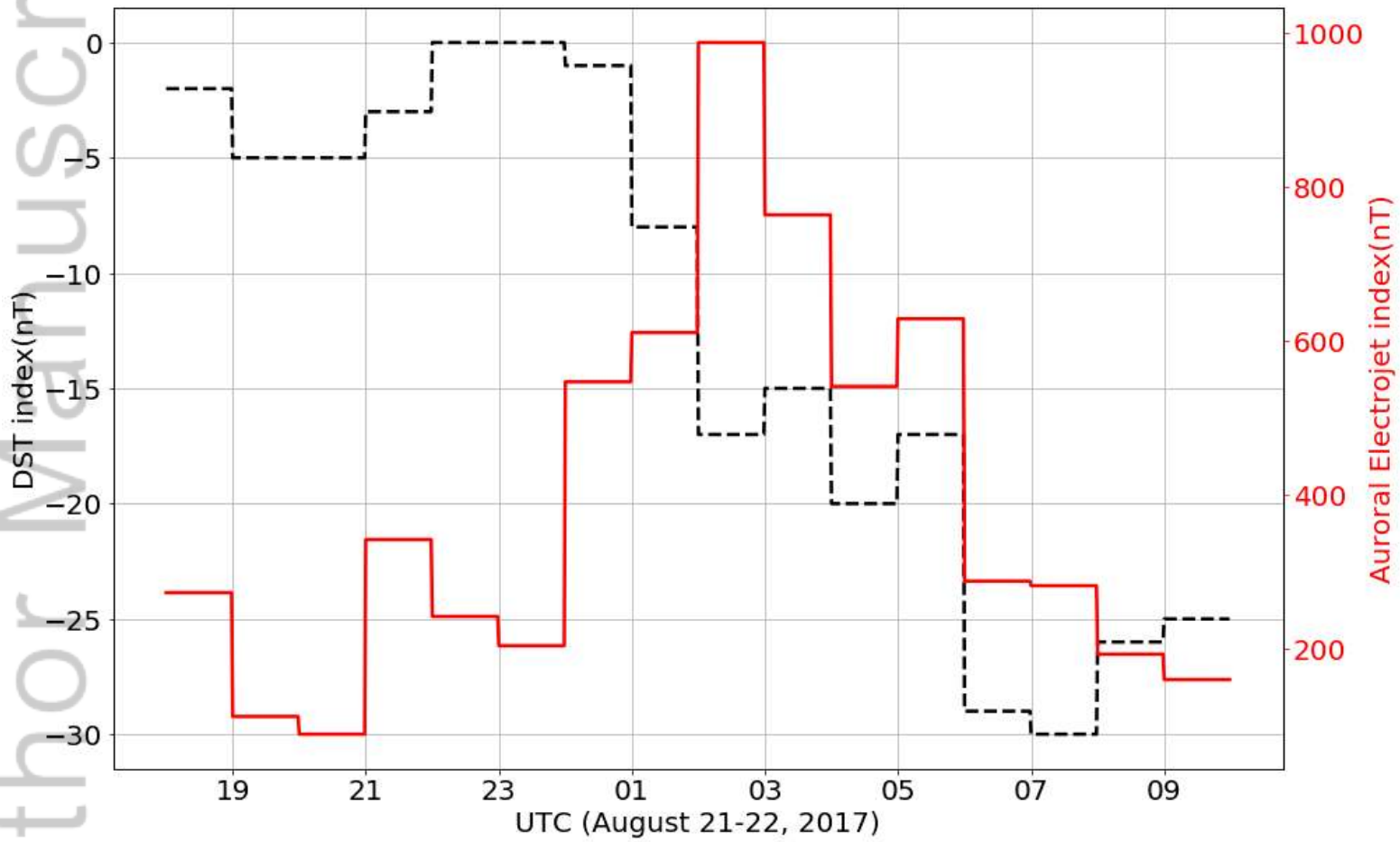
Differential TEC at Carbondale, IL on August 22, 2017



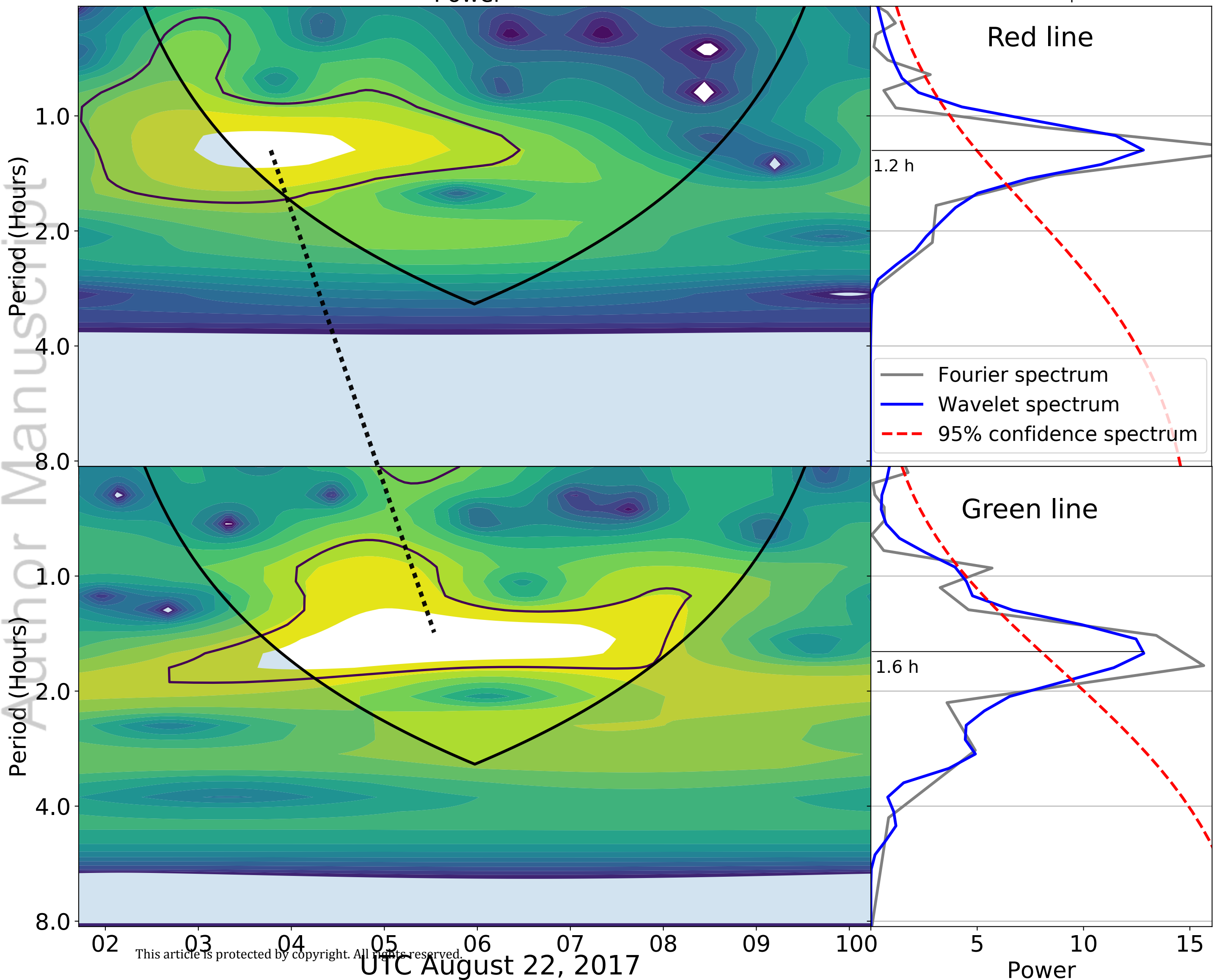
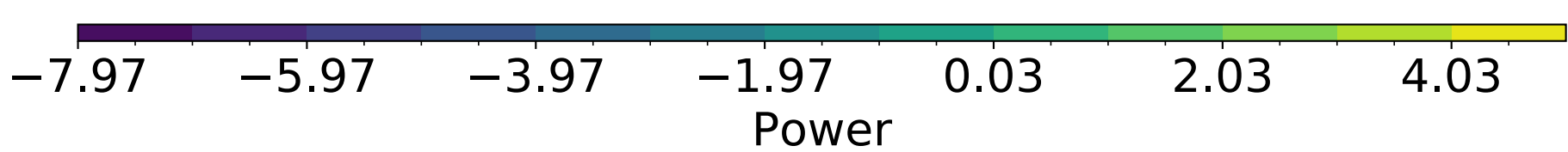
2018JA026333-f05-z-.png

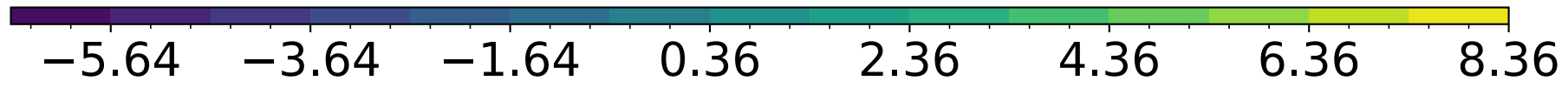


2018JA026333-f06-z-.png

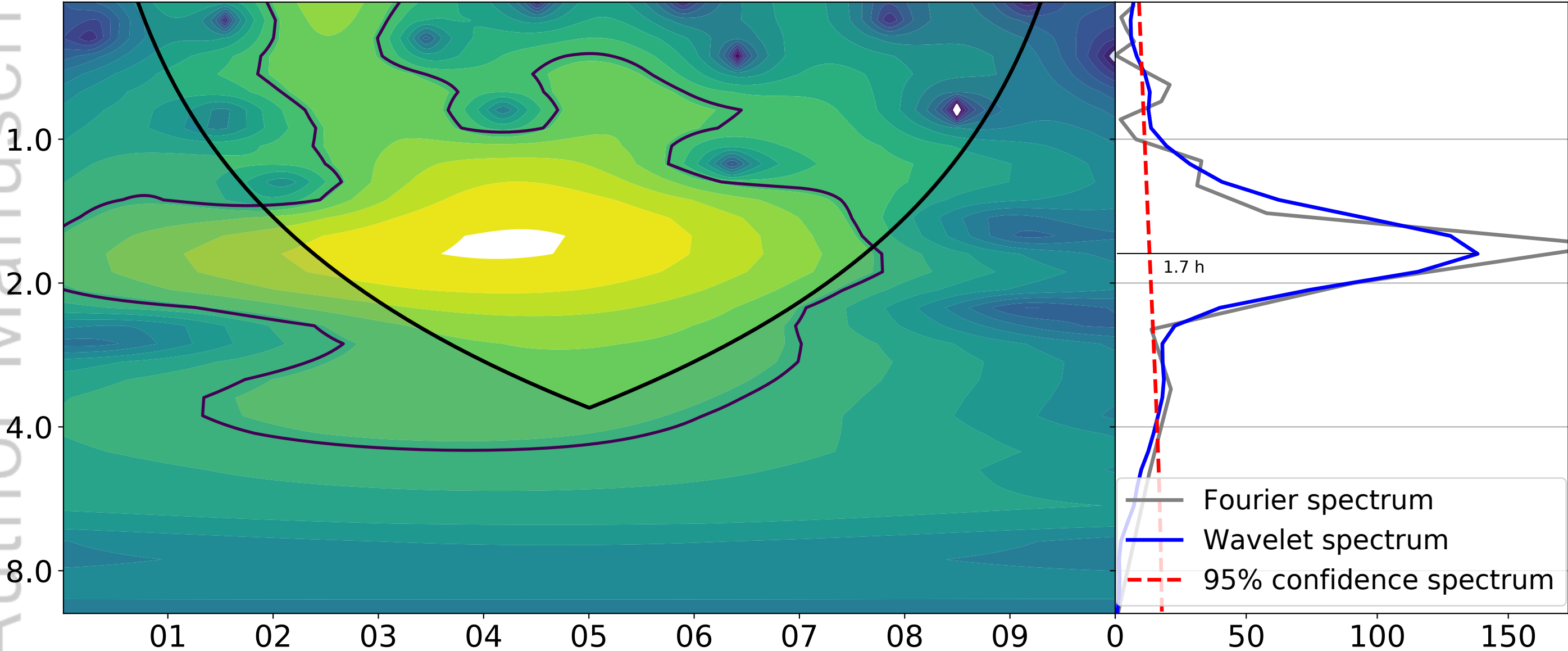


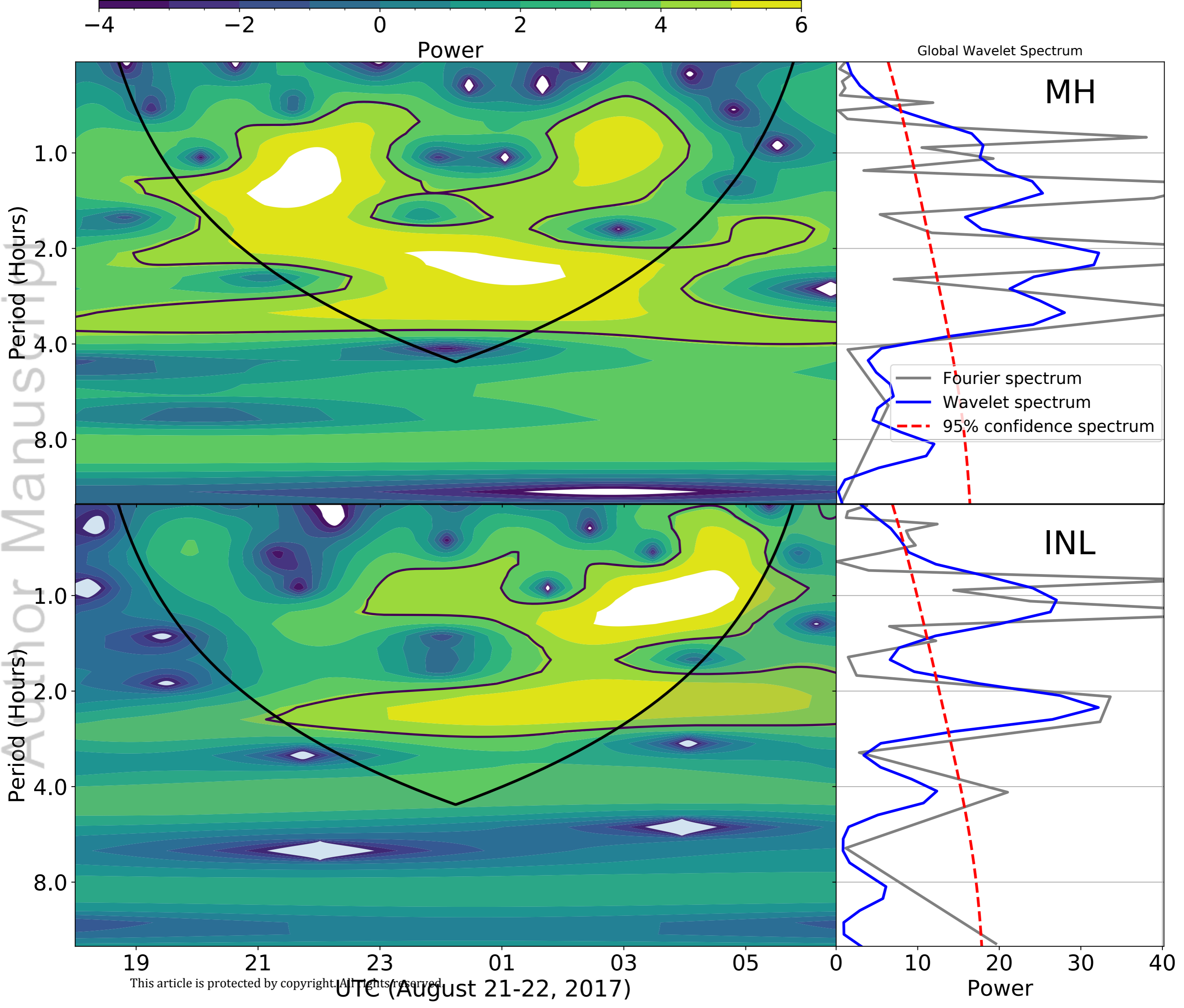
2018JA026333-f07-z-.png

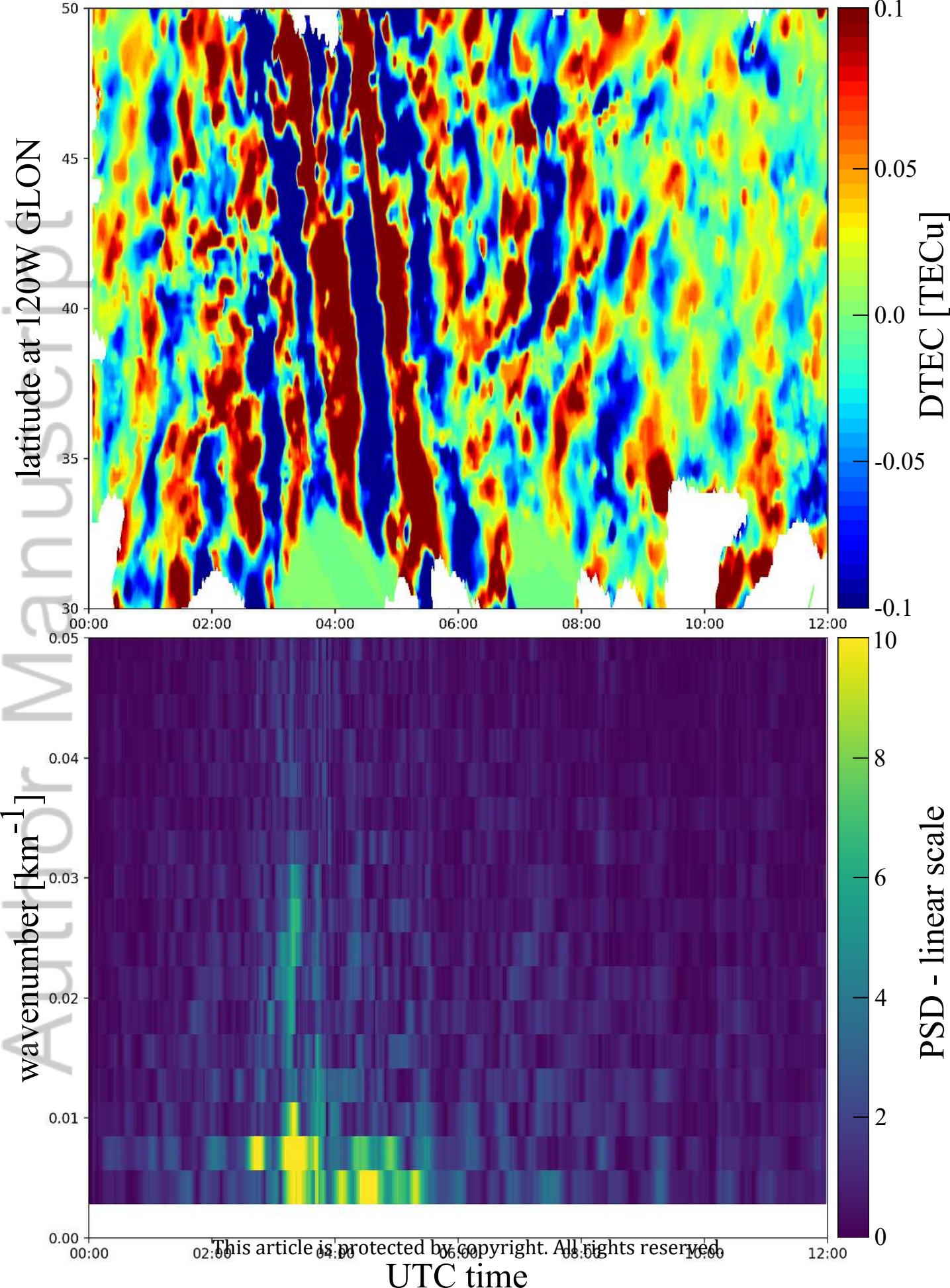




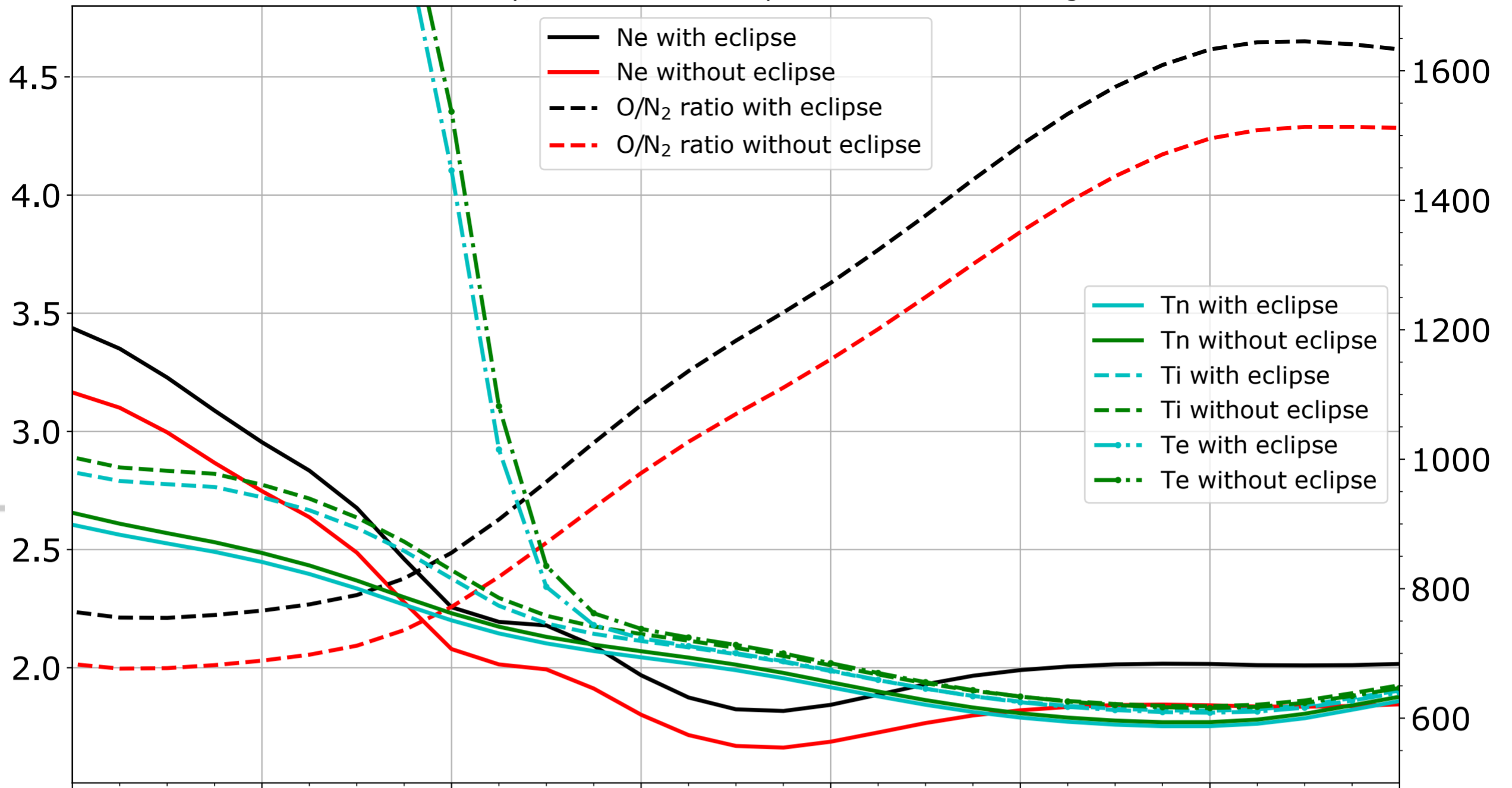
Global Wavelet Spectrum







Electron Density, O/N₂ ratio and temperatures at 250 km using GITM



Electron Density, O/N₂ ratio and temperatures with constant IMF at 250 km using GITM

